



ND280 Upgrade Project: Addendum to T2K ND280 Upgrade Technical Design Report

The T2K ND280 Upgrade Working Group

Abstract

This document is an Addendum to the TDR for the upgrade of the Near Detector of the T2K experiment, prepared for the KEK/IPNS review committee.

Following the review committee recommendations, we present a detailed description of the Super-FGD assembly method and we show sensitivity studies intended to further demonstrate the physics capabilities of ND280 upgrade.

Version 2.0
June 19, 2020



Contents

1	T2K and the ND280 upgrade project	3
2	Project progresses	3
2.1	The Super-FGD	4
2.1.1	Cubes production and Layers assembly at INR	4
2.1.2	Mechanical box and sagging tests	4
2.1.3	Wavelength Shifting fibers, MPPCs and calibration system	6
2.1.4	Super-FGD electronics	7
2.1.5	Performance Studies with Prototypes	8
2.1.6	CERN Testbeam Studies	9
2.1.7	Neutron beam tests at LANL	9
2.1.8	Next steps	10
2.2	The High Angle TPCs	10
2.2.1	ERAM modules and DESY test beam	10
2.2.2	First TPC Field Cage prototype	11
2.2.3	Prototype cosmics tests at CERN	13
2.2.4	Final TPC field cage design	14
2.2.5	Gas system	14
2.2.6	TPC electronics	14
2.2.7	Next steps	14
2.3	The Time Of Flight detector	15
2.3.1	Next steps	16
2.4	Detector Installation	16
2.5	Project Time Schedule	17
3	Super-FGD Assembly method	18
3.1	Fishing Line Method	19
3.2	Cube Array Assembly	19
3.3	Cube Layer Assembly	20
3.4	Super-FGD Volume Assembly Test using Prototypes	21
3.5	Fiber Insertion Test with Controlled Detector Sagging	21
3.6	Full-size Super-FGD Assembly	24
3.7	Super-FGD Assembly Time Line	25
3.8	Ultrasonic Welding Assembly Method	25
4	Sensitivity studies	27
4.1	Prospects for the T2K oscillation analysis	28
4.2	Physics potential with low momentum protons and neutrons	31
4.2.1	Reduction of key model uncertainties	33
4.2.2	Anti-neutrino energy reconstruction from $\bar{\nu}_\mu$ interactions on hydrogen	35
4.2.3	Improvements on ν_e/ν_μ uncertainty	37

1 T2K and the ND280 upgrade project

The T2K experiment is a long-baseline neutrino oscillation experiment, currently ongoing in Japan. T2K has been the first experiment to detect the appearance of electron neutrinos in a muon neutrino beam and is now searching for CP violation in the leptonic sector by precisely measuring appearance probabilities of neutrino and antineutrinos. Such measurement requires both, larger statistics and a better understanding of systematic uncertainties. In order to improve the latter, an upgrade of the T2K Near Detector, ND280, is being conducted and is expected to significantly reduce the impact of systematic uncertainties on T2K oscillation analyses and, more in general, to improve the current knowledge of neutrino cross-section models.

The ND280 upgrade, shown in Fig. 1, will consist in replacing one of the sub-detectors, the POD, the most upstream inner detector of ND280, with two horizontal TPCs (HA-TPC) and a horizontal fully active carbon target in the middle (Super-FGD). Six Time-of-Flight (ToF) planes will be installed around the HA-TPCs and the Super-FGD.

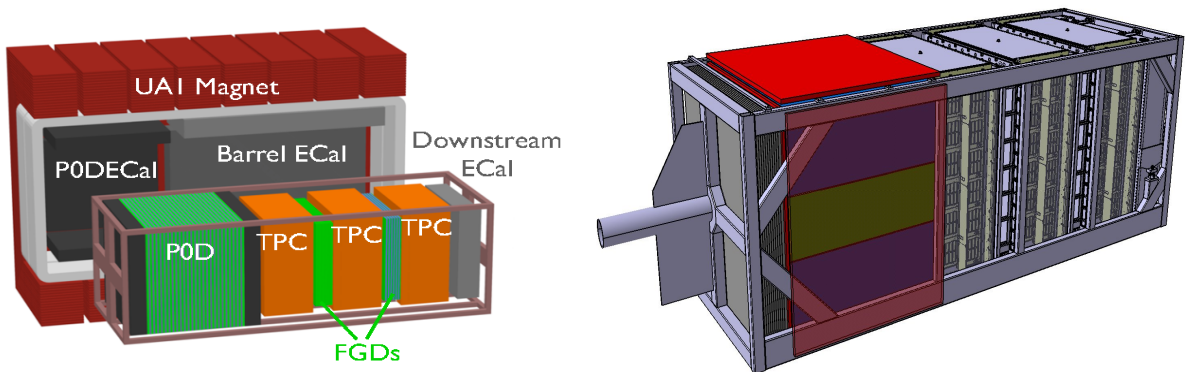


Figure 1: Left: Sketch of the current ND280 detector. Right: Sketch of the ND280 upgrade project, including Super-FGD (green), HA-TPC (violet) and ToF modules (red).

These detectors are being constructed and will be assembled, mostly at CERN, in 2020 and 2021 before being shipped to Japan in the second half of 2021. The main improvements that will be obtained thanks to the upgrade with respect to the current Near Detector configuration (see Fig. 2) are:

- higher efficiency in reconstructing muons produced in neutrino interactions and emitted at high polar angle with respect to the neutrino direction, thanks to the two high angle TPCs.
- higher efficiency in detecting low momentum protons and pions produced in neutrino interactions thanks to the high granularity and the 3D reconstruction capabilities of the Super-FGD .

At the end of 2018 we submitted a TDR describing the ND280 upgrade [1]. Such document has been reviewed by the KEK IPNS review committee, by the J-PARC PAC and by the CERN SPSC. Following the positive recommendations from the SPSC, the ND280 upgrade became, in April 2019, one of the approved projects in the CERN Neutrino Platform (NP07). This document is an addendum of the TDR and it consists of three sections. In Sect. 2 we review the main progresses of the ND280 upgrade since the publication of the TDR, in Sect. 3 we review the Super-FGD assembly method that was one of the main question raised by the KEK IPNS review committee. Finally, in Sect. 4 we present some new ND280 sensitivity studies, not shown in the original TDR.

2 Project progresses

In this section we review the progresses for the different subdetectors since the publication of the TDR [1] at the end of 2018.

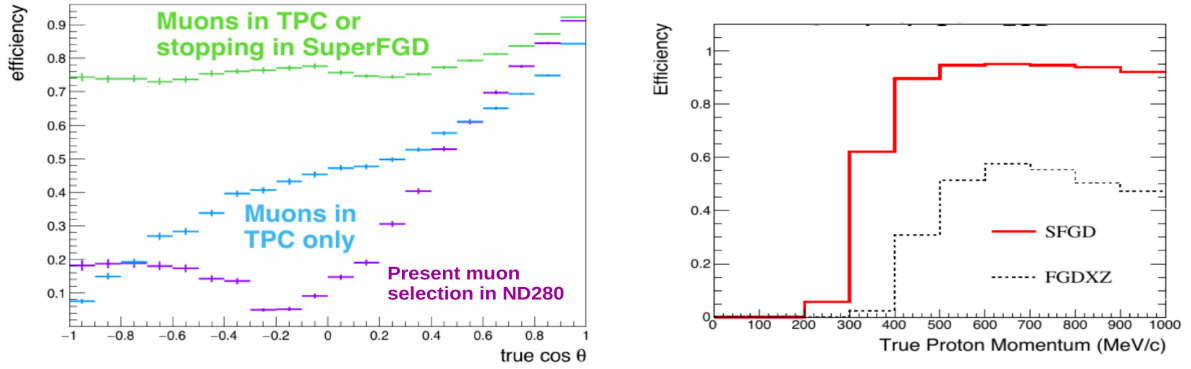


Figure 2: ND280 upgrade efficiency in reconstructing muons (left) and protons (right).

2.1 The Super-FGD

The Super-FGD is a novel design of fine grained fully active plastic scintillator detector and it consists of ~ 2 millions of optically independent cubes of plastic scintillator, read out along three orthogonal directions by wavelength shifting (WLS) fibers, coupled at one end with a Multi-Pixel Photon Counter (MPPC). The active part consists of $192 \times 184 \times 56$ cubes, with the size of each cube of $1 \times 1 \times 1$ cm³. The total weight of the Super-FGD will be ~ 2 tons.

2.1.1 CUBES PRODUCTION AND LAYERS ASSEMBLY AT INR

The scintillator cubes are produced at UNIPLAST Co. (Vladimir, Russia) at a stable rate of ~ 100 k cubes per month. The size uniformity of the cubes is excellent, with $\sigma \sim 30$ μ m.

Slightly larger variations, of the order of $\sigma \sim 50$ μ m are observed for the hole positions drilled to insert WLS fibers through a cube.

After drilling the holes, the cubes are delivered to INR (Moscow) where a quality check is performed, checking that stainless steel needles can be inserted in all the three directions. This quality check rejects $\sim 5 - 7\%$ of the cubes. Total of 1.26 million cubes have been already delivered to INR; at this rate, it is expected that the production of cubes will be completed by the end of 2020.

The cubes passing the quality check are assembled in xy layers with fishing lines. The full chain from the quality check to the assembly of the xy layer is shown in Fig. 3. By the middle of May 2020, 28 full-size layers (192×184 cubes) had been assembled. In addition, in order to test the sagging of the Super-FGD, 56 narrow-size layers (192×15 cubes) have been assembled together into a tower as shown in Fig. 4. Such tower corresponds to the full height of the Super-FGD and the cubes used to assemble it are equivalent to 4.5 full-size layers.

2.1.2 MECHANICAL BOX AND SAGGING TESTS

The Super-FGD cubes will be installed inside a mechanical box, consisting of six panels. A detailed description of the assembly procedure will be given in Sect. 3.

Each panel will host an AIREX foam within two thin Carbon Fiber (CF) layers. Each panel has 3 mm diameter holes spaced in a pitch of about 1 cm to allow passing the WLS fibers outside the CF box. The WLS fibers are then attached to the plastic layer with optical connectors pressurized by soft foam to ensure the contact between the fiber ends and the MPPC channels. MPPC channels are soldered on PCB with 8×8 MPPCs array and the PCB is screwed on the box.

The design of the optical connectors has been finalized and we are ready to start the procurement while for the box, we are actively working on the finalization of the design and the fixation system to the basket.

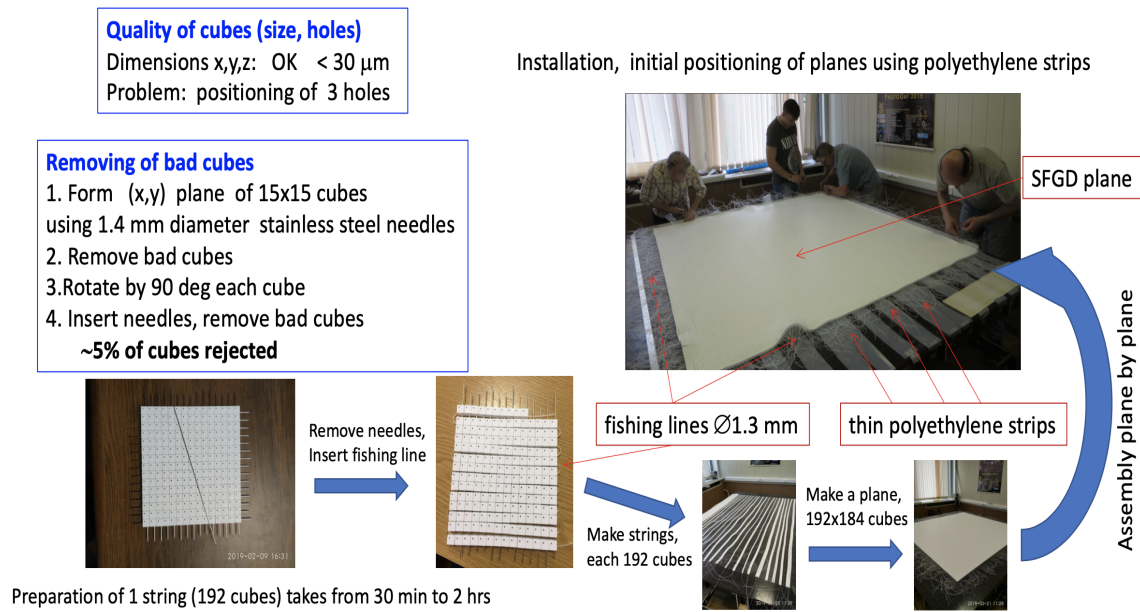


Figure 3: From the quality check of the Super-FGD cubes to the assembly of one xy layer with fishing lines.



Figure 4: 56 narrow-size layers of cubes assembled together into a tower for the sagging measurements.

According to FEA analysis, we expect that the weight of the Super-FGD will induce a sagging of 3–4 mm in the center of the detector. The simulation model has been validated with a prototype of the bottom layer of the box of 15 (w) x 192 (l) cm². During the tests carried out at INR, the tower shown in Fig. 4 have been mounted on the box prototype and the sagging has been measured for different number of layers. The measurements confirmed the results of the FEA simulations, including the fact that, once the holes are drilled on the box, the sagging increases by ~ 20%. The results of these tests are shown in Fig. 6.

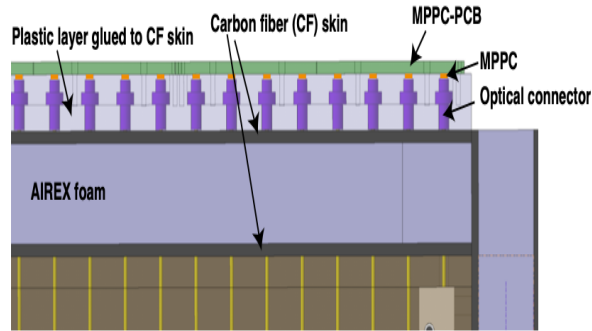


Figure 5: Design of the Super-FGD box and connection to the MPPCs.

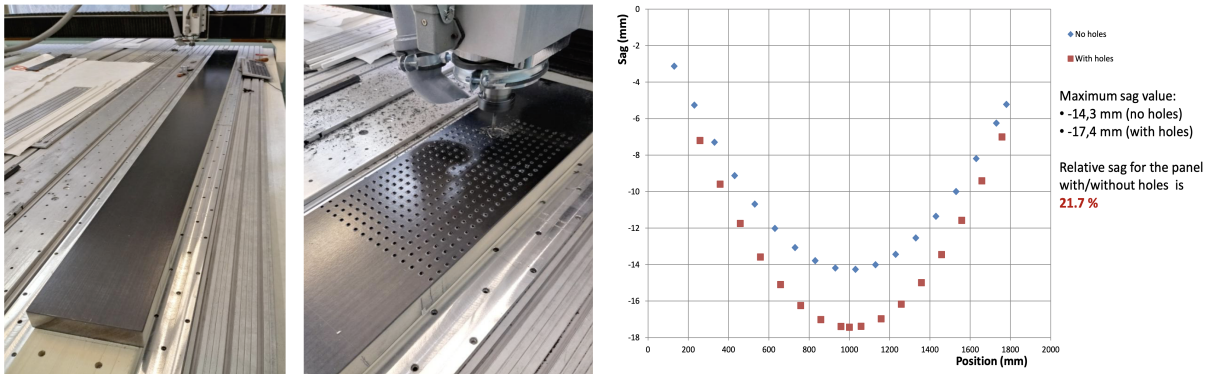


Figure 6: Drilling of holes in the Super-FGD box prototype (left). 15×192 holes with 3.0 mm diameter and with a step of 10.3 mm have been drilled. The measured sagging as a function of the position with and without holes are shown on the right plot.

2.1.3 WAVELENGTH SHIFTING FIBERS, MPPCS AND CALIBRATION SYSTEM

In order to instrument the Super-FGD we will need 73 km of fibers (including the spare) and $\sim 63k$ MPPCs that will be mounted on PCBs. Each PCB will host 64 MPPCs. For the fibers, the procurement is being organized and, before launching the mass production, we are finalizing the decision for the treatment of the end surface of the fibers with measurements from test benches.

Concerning the MPPCs, 50 k of them have been already delivered from Hamamatsu in Japan and the remaining 13 k will be delivered in the US. First measurements of MPPCs operation voltage with a prototype PCB have been performed, as shown in Fig. 7. The small variation in the operation voltage seen in Fig. 7 is due to the feature of measurement system and not PCB board design. Measurement with an independent system does not show this variation. The final electronics will be designed not to show this kind of characteristic variation. In any case, the amount of observed difference is small enough so that it can be calibrated and adjusted by the Super-FGD electronics.

A Test Bench, that will allow to characterize eight PCBs simultaneously in term of gain and dark noise rate using an LED system and a Light Guide Plate (LGP) is being designed. Thanks to this system, the full characterization of the MPPCs is expected to be completed by March 2021.

A calibration system is also being designed for the Super-FGD, with an LED emitting light that is collected by the WLS fibers on the side not connected to the MPPCs. Such system has the purpose of providing regular calibration of MPPCs gain during the long-term operations. The main option foresees the LEDs mounted on a PCB on the bottom of the Super-FGD, to minimize interference with the fixation system to the basket. The light will then be distributed to the fibers through an LGP as shown in Fig. 8. Tests on prototype have shown that a light uniformity over all the WLS fibers from the

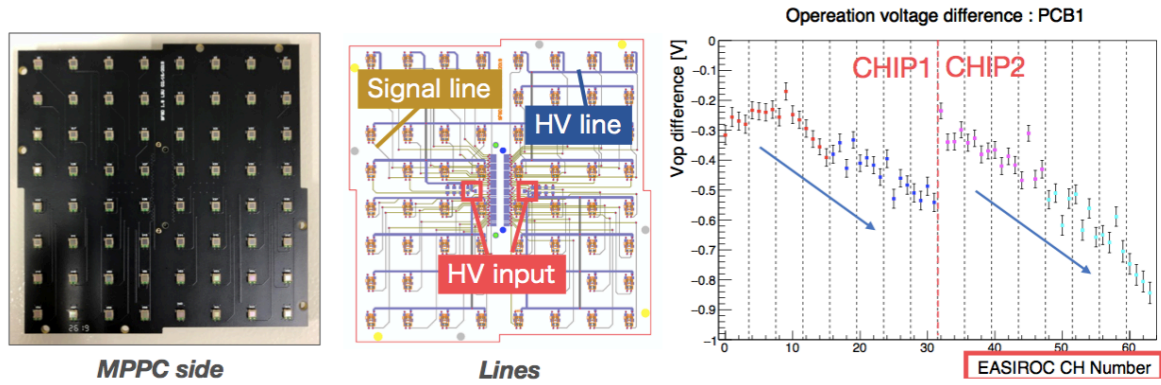


Figure 7: Design of the MPPC PCB and measured difference in the operation voltage between the MPPCs mounted on the PCB and the one measured by Hamamatsu.

same LGP within a factor of 2 can be obtained with this system. We expect to complete the design of the LED calibration system by April 2020.

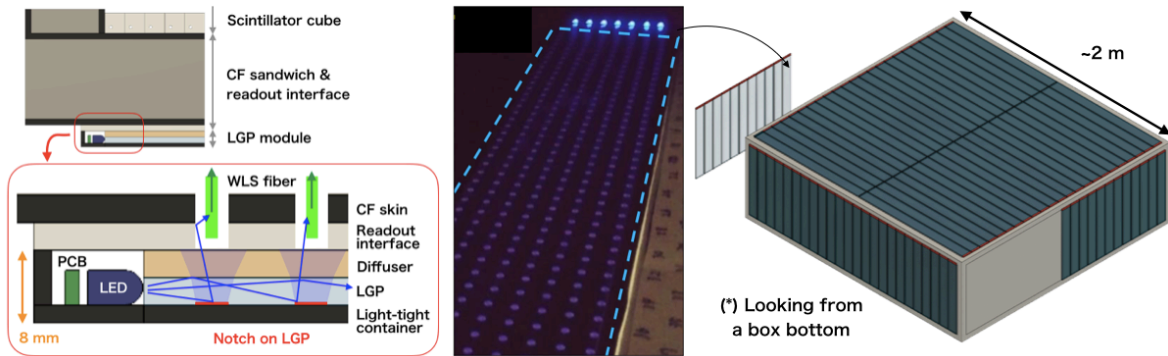


Figure 8: Design of the LED calibration system (left). The optical system is modularized as found in the middle picture and integrated to the mechanical box (right).

2.1.4 SUPER-FGD ELECTRONICS

The electronics engineers from LLR, University of Geneva and US groups (University of Pennsylvania and University of Pittsburgh) are working on finalizing the design of the Super-FGD electronics. The CITIROC chip has been chosen for the SiPM readout. Such a chip has the advantage of being well established, also used in commercial products. The Front End Boards are being designed, based on the one designed by the team at the University of Geneva for the Baby-MIND detector, which is presently being used as a part of the WAGASCI setup taking data in the ND280 pit. In order to cope with the very small space available and to reduce power dissipation, the new design requires extending the Baby-MIND one from 3 to 8 CITIROC chips, which corresponds to 96 to 256 channels.

The front end electronics will therefore be composed of 221 Front-End Boards (FEBs), each of them embedding 8 CITIROC chips, 2 ADCs and one (Intel)Arria-10 FPGA. A block diagram of these new Front End Boards can be seen on Fig. 9. All required chips have been acquired from Weeroc (France) and will be delivered in the coming months. The FEBs will be installed in 16 crates mounted in the basket (8 on each side of the Super-FGD). The analog signals from the MPPC boards will be conveyed to the FEBs using SAMTEC flat ribbons containing 80 micro-coaxial cables each, as can be seen on Fig. 10-Left. These cables will be connected on the "front" of the FEBs (corresponding to the outermost side of the crates), by means of a small dedicated board, in order to ensure an easy and

safe connection with no need to fold the cables. Each crate (see Fig. 10-Right) will host an Optical Concentrator Card (OCC) that will control 14 FEBs and send their data to the DAQ by means of optical fibers. In each crate, the OCC communication with the FEBs will be ensured by a dedicated backplane located on the innermost side of the crate.

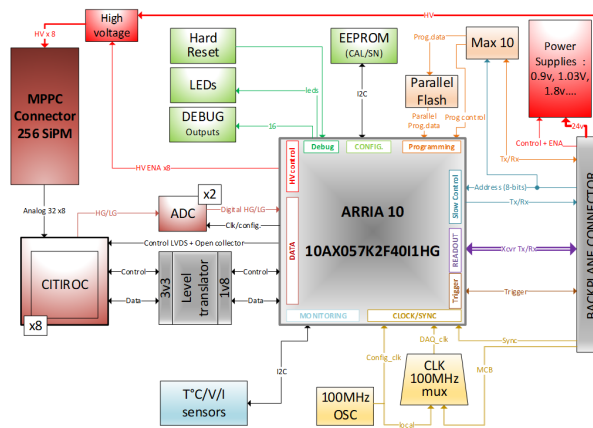


Figure 9: Simplified block diagram of a Front-End Board. The Arria-10 FPGA will ensure the control of 8 CITIROC chips, and the digitization of the analog signals through 2 ADCs. It will also ensure all communications with the OCC through the back-plane connection.

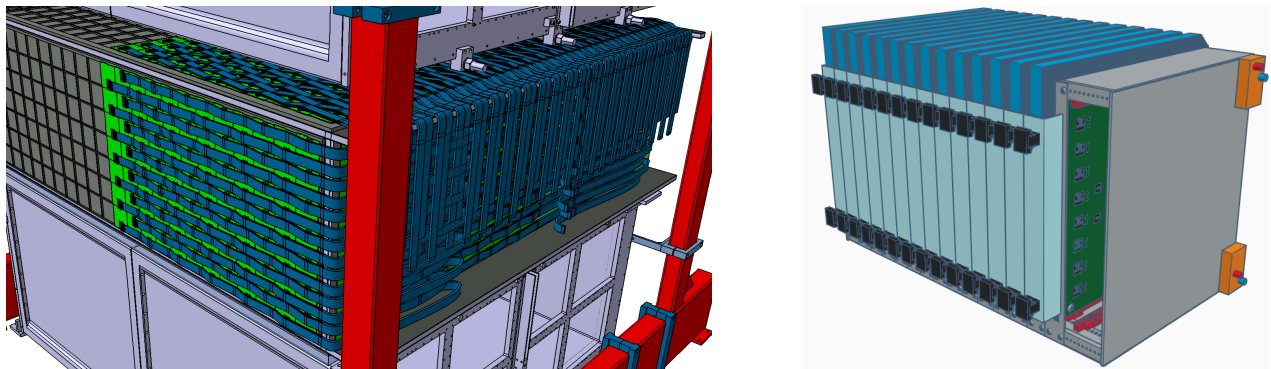


Figure 10: Left: Schematic view of the Super-FGD detector, showing the flat SAMTEC cables conveying the analog signals from the MPPC boards to the FEBs. Right: Schematic view of a crate containing 14 FEBs and a large slot dedicated to the OCC. Two rows of 4 crates will be located on each side of the Super-FGD. The flat cables will be running on the top of the top row, and on the bottom of the bottom row. As shown here, dedicated plugs, hosting printed circuit boards, will be designed to ensure easy and safe connection of the bundle of cables to the front panel of the FEBs.

2.1.5 PERFORMANCE STUDIES WITH PROTOTYPES

Two Super-FGD prototypes have already been constructed and instrumented. The first Super-FGD prototype, assembled at CERN, has 9216 cubes which are read out by 1728 MPPCs. As electronics the one developed for the Baby MIND project was used. It has same CITIROC chips adopted for the Super-FGD electronics. The second prototype, assembled in the US, has 2048 cubes and 576 channels and is read by MPPCs. Its design already takes into account several of the design concepts considered for the final Super-FGD. For example the MPPCs are mounted on PCB in group of 64, as in the final Super-FGD design. It also uses the Baby MIND electronics for the readout.

2.1.6 CERN TESTBEAM STUDIES

The first prototype was exposed in summer 2018 during two campaigns to a particle beam at the T9 station at CERN. A dedicated trigger system was set up by the collaboration allowing to select different particle types. This was used to study the detector response to these particles with and without magnetic field. An event display showing a photon conversion is shown in fig 11. Fig 12 shows the energy deposited by protons, pions and positrons measured with the SuperFGD prototype. It is also shown that the already very good particle identification by dE/dx can be enhanced by precisely measuring the particle range. The Bragg peak of a stopping proton is shown in fig. 13. The publication of the results is expected to be submitted before June.

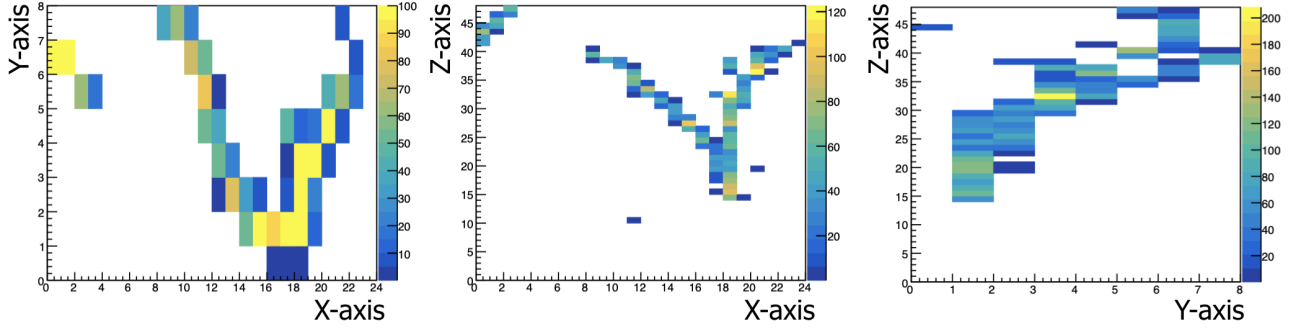


Figure 11: Event display showing a photon converting in the Super-FGD prototype during the beam test at CERN. The prototype was surrounded by a 0.2 T magnetic field.

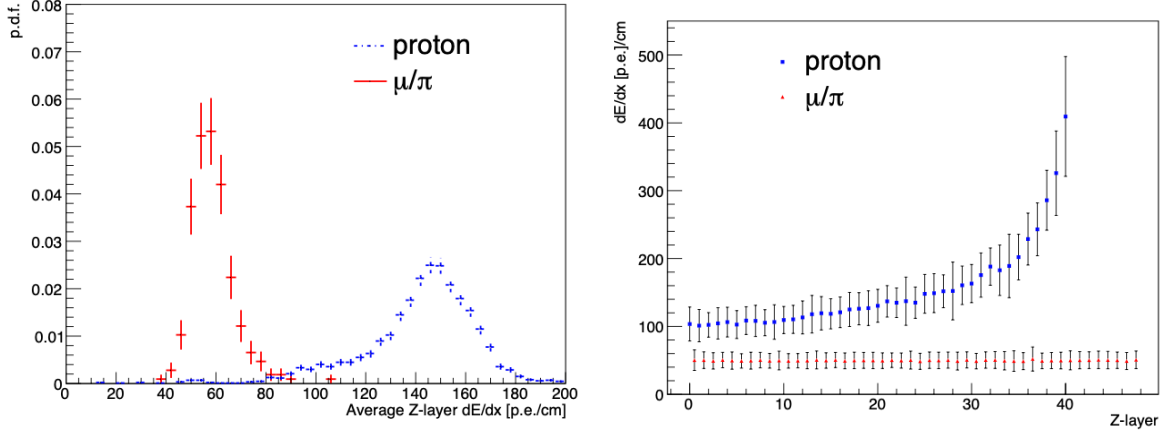


Figure 12: **Left:** Distribution of dE/dx for protons stopping in SuperFGD and pions and muons crossing the detector. No cuts on the particle track length is applied. **Right:** Measured average dE/dx as a function of the particle track length in the SuperFGD prototype for protons and pions.

2.1.7 NEUTRON BEAM TESTS AT LANL

The detector response to neutrons is of special interest to measure anti-neutrino interactions ($\nu + p \rightarrow l^+ + n$) in the detector. Two Super-FGD prototypes have been exposed, in December 2019, to a neutron beam at the Los Alamos National Laboratory to study the detector response to this type of particle. The beam emits neutrons with energy up to 800 MeV produced by protons impinging on a tungsten target. The beam is pulsed, allowing for the selection of the neutrons based on Time Of Flight.

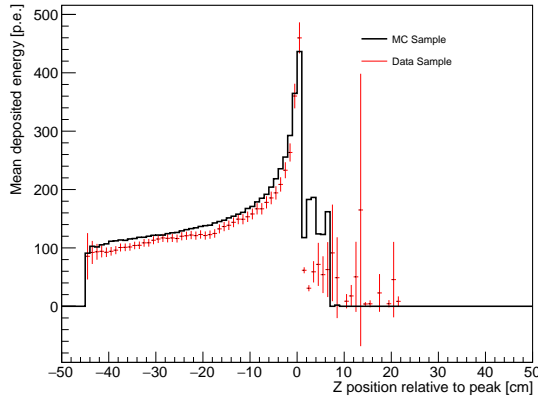


Figure 13: Measured dE/dx of protons stopping in the SuperFGD prototype. The data (red) are compared with simulations (black).

Data have been taken in two locations, at 90 m and at 20 m from the target and will allow to characterize the response of the Super-FGD to neutrons. The analysis of the data is on-going and the possibility of another test beam campaign in Fall 2020 is being considered.

2.1.8 NEXT STEPS

The next critical milestone for the Super-FGD project is the finalization of the design and the production of the assembly box, that should be delivered to CERN by September 2020 in order to timely start the assembly of the xy cube layers that will be shipped from INR in the coming months.

The assembly at CERN will be done with fishing line and, once completed, we will ship the Super-FGD to J-PARC where the fishing line will be replaced with WLS and the MPPC PCB will be installed.

2.2 The High Angle TPCs

The HA-TPC shares many features with the existing ND280 TPCs, that has so far obtained completely satisfying performances. The two main innovations with respect to the existing TPCs will be the use of Resistive MicroMegas modules, called ERAM (Encapsulated Resistive Anode MicroMegas) and the use of a single layer of solid insulator laminated on a composite material for the field cage, while for the current ND280 TPCs, two gas-tight boxes, one inside the other were used.

The ERAM modules, naturally introduces a spread in the charge on the anode plane, allowing for a lower density of readout pads and eliminating the risks of discharges (sparks). This allows to remove the protecting diodes on the front end cards. The new design of the field cage, instead, minimize the dead space and maximize the tracking volume.

2.2.1 ERAM MODULES AND DESY TEST BEAM

So far we have tested two MicroMegas modules. The first one (MM#0), based on the layout of the existing TPC MicroMegas but with the addition of a resistive foil has been test in the HARP field cage during a Test Beam campaign at CERN in 2018 and the results have been published in [2]. The performances in terms of deposited energy resolution and spatial resolution are shown in Fig. 15.

The second module (MM#1), with the layout conceived for the HA-TPC (1152 pads, with dimensions of 10.1×11.2 mm) has been tested in a Test Beam at DESY in 2019. It should be noted that thanks to the superior performances of the resistive technique, a reduction in the total number of channels of 33% is obtained.

Parameter	Value
Overall $x \times y \times z$ (m)	$2.0 \times 0.8 \times 1.8$
Drift distance (cm)	90
Magnetic Field (T)	0.2
Electric field (V/cm)	275
Gas Ar-CF ₄ -iC ₄ H ₁₀ (%)	95 - 3 - 2
Drift Velocity $cm/\mu s$	7.8
Transverse diffusion ($\mu m/\sqrt{cm}$)	265
Micromegas gain	1000
Micromegas dim. $z \times y$ (mm)	340×410
Pad $z \times y$ (mm)	10×11
N pads	36864
el. noise (ENC)	800
S/N	100
Sampling frequency (MHz)	25
N time samples	511

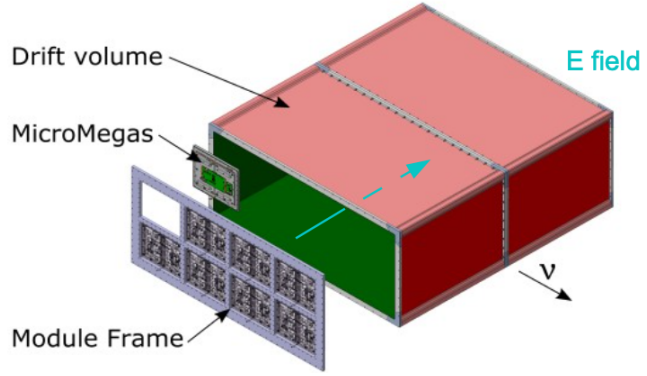


Figure 14: Parameters and sketch of the new HA-TPC.

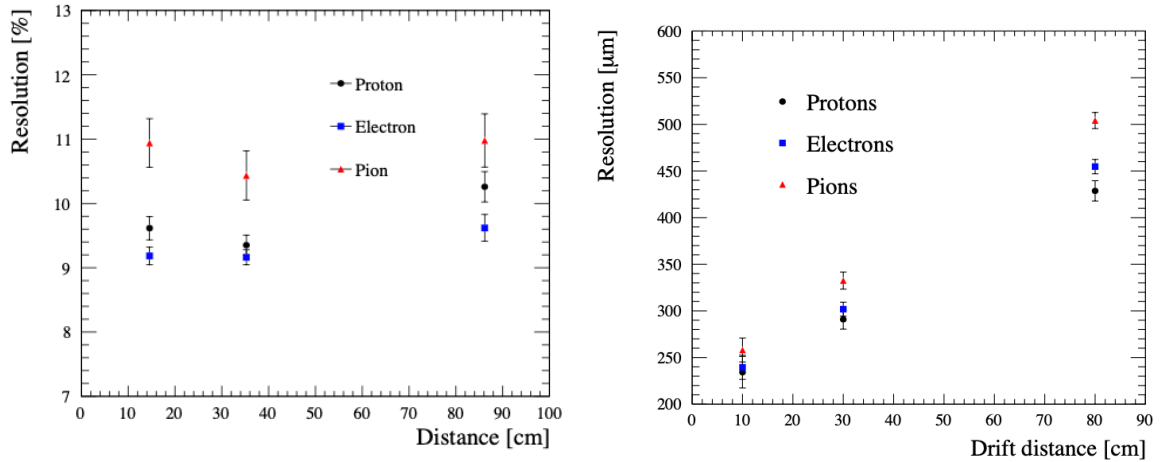


Figure 15: Deposited energy resolution (left) and spatial resolution (right) for the MM#0 module tested at CERN in 2018.

The tests at DESY have been done in a short chamber (15 cm drift distance) with electrons of 4 GeV/c and with and without magnetic field. The test beam allowed to characterize and validate the design of the new detector and to make precise measurement of the resistivity of the module as a function of the pad position.

The results of these test beams allowed to launch the production of the pre-series of the ERAM modules (see Fig. 16). These modules will have the same design of MM#1 except for the fact that the thickness of the glue will be increased from 75 to 200 μm , in order to decrease RC and increase the spread of the charge.

The first ERAM module to be used in the HA-TPC have been delivered at Saclay in February 2020 and it will be followed by 7 additional modules for which the DLC foils have been received by B-Sputter.

2.2.2 FIRST TPC FIELD CAGE PROTOTYPE

The TPC field cage is designed as a single box structure, with the walls made of insulator. The box also makes up the field cage and two drift volumes are defined by a central common cathode. On the other side the volumes are closed by an anode supporting the 8 ERAM modules mounted on a module frame.

In 2019 we produced and tested one small scale prototype that has the same drift length of the final TPC (1 m) but smaller transverse dimension (43×43 cm), suitable for the installation of one ERAM module. The prototype, shown in Fig. 17, has been manufactured by NEXUS (Barcelona) and tested in

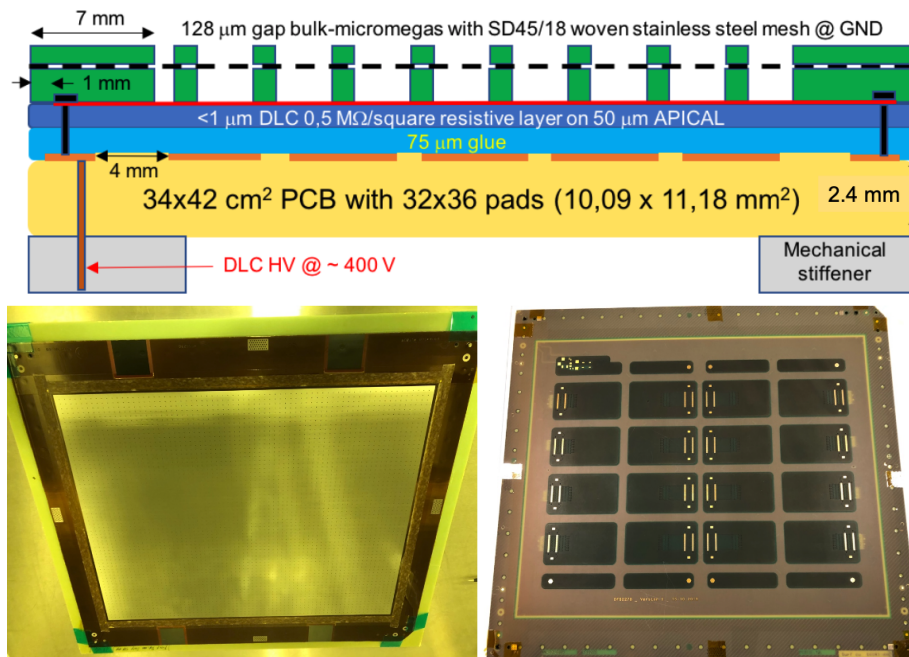
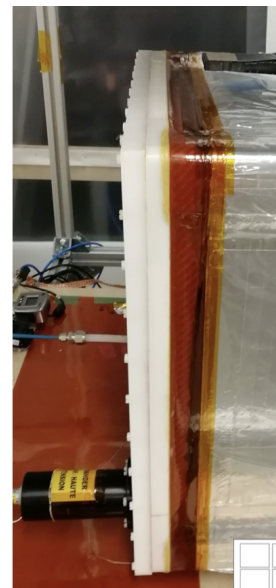
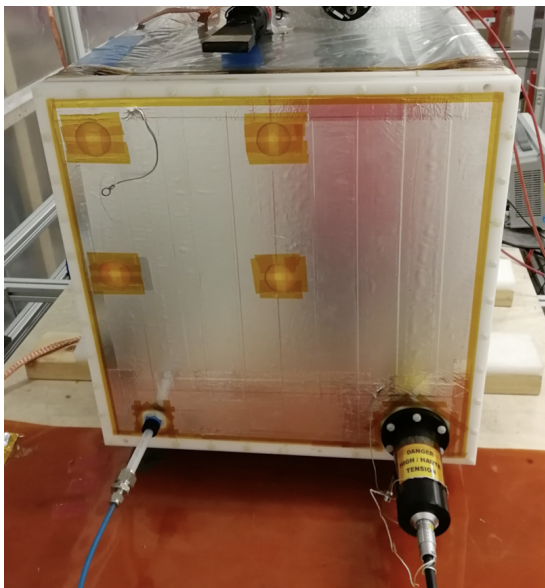


Figure 16: Schematic cross-section of a resistive MicroMegas module and photo of the first ERAM module produced.

Air at Legnaro before being moved to CERN.



Aramid Fiber fabric based layer stack

	Material	Thickss (mm)
outer layer	Aluminum coated polyimide film	~ 0.15
	Aramid Fiber Fabric (Kevlar)	2.00
	Aramid HoneyComb panel	35.00
inner layer	Aramid Fiber Fabric (Kevlar)	2.00
	Polyimide film (insulation)	~ 0.10
	Strips (double later) on Kapton foil	~ 0.15
	TOTAL RADIATION LENGHT - 4% X0	~ 39.40

Figure 17: First TPC prototype.

Some issues were observed concerning the mechanical rigidity, the electrical aspects and the gas tightness and are reported below. Following these findings, the design of the TPC field cage has been slightly changed as it will be reported in 2.2.4.

Mechanical aspects

During the measurements done at Legnaro ~ 20 bubbles were observed, due to air trapped along the kapton valley between strips. These bubbles can be cured by doing a tiny hole, sucking the air with a

syringe and sealing the hole with Kapton tape.

In Legnaro we also measured the flatness of the prototype field cage shapes, with maximal deviations of $200\ \mu\text{m}$ for the inner surface, $300\ \mu\text{m}$ for the flange plane. The transverse cross section shape is constant with deviation from a square shape of $800\ \mu\text{m}$. Such values are well within the requirements that were given for the HA-TPC.

Electrical aspects

Some interruptions of electrical continuity have been found in the first prototype in the field strips. These were spotted while checking the resistance of the strip between the two strip ends and were cured for the prototype by using small samples of strip foils to bridge the interruption.

Such interruptions were not found in the mirror strip, although one short circuit between 2 not adjacent mirror strip was found, precisely located and cured. The risks of such short will be mitigated in the future by adding a kapton layer between the strip foils and the Twaron layer.

Gas Tightness

One of the main issues with the prototype was its gas tightness, with gas leaks at the level of 30 l/h. During the visual inspection we spotted some sources of leaks due to the difficulties in gluing the POM-C that was used for this first prototype.

This particularly affects the flanges and, after the results of the prototype, we decided to use G10 instead of POM-C. G10 is much easier to glue and, in order to test the gas tightness, we produced a small prototype of field cage using G10 for the flanges at ORVIM, Venice, in which the gas leak was below 1 l/h.

2.2.3 PROTOTYPE COSMICS TESTS AT CERN

After these tests the TPC prototype was moved to CERN where the T2K gas mixture was fluxed inside the Field Cage and High Voltage tests were performed. At the begin some sparks had been observed in the region close to the cathode and were solved by properly shaping the external grounded shielding. After this fix it was possible to operate the TPC at an HV of 18 kV for several days. Tests at higher voltages were also performed, and stable operations were possible at the design value of 25 kV.

The analyses of these cosmics data is on-going and some preliminary results are shown in Fig. 18.

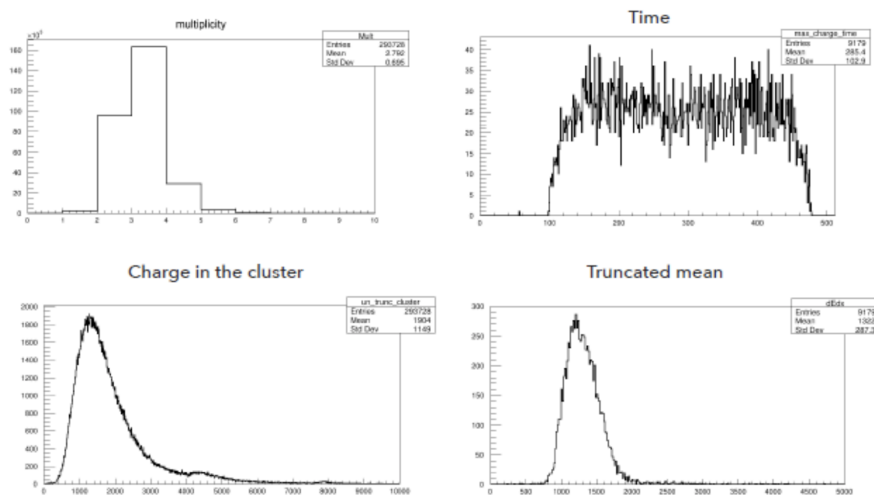


Figure 18: Measurements with the TPC prototype at CERN: Cluster multiplicity (top left), arrival time (top right), charge per cluster (bottom left) and charge truncated mean (bottom right).

2.2.4 FINAL TPC FIELD CAGE DESIGN

Taking into account the results from the first TPC prototype, it has been decided to review the design of the field cage in order to improve the fabrication process and reduce the risk of leaks. In particular we will use G10 instead of thermoplastic (far easier to glue and stiffer) and we will produce a single-piece G10 flange, in order to reduce the needs for screws. The procedure for the strip-layer placing system at NEXUS have been improved, based on the results of the first prototype and a new insulating Kapton layer between the strips and the Twaron layers will be added to reduce the risks of shorts.

Also the design of the mold has been improved in order to avoid blisters on the strip faces and to reduce the possibility of damages during the dismounting of the mold. All these changes have been agreed with NEXUS and will be tested in a second prototype, of the same size of the first one, that will be delivered by NEXUS by Summer 2020.

An external review of the TPC field cage has been organized by the T2K Executive Committee in order to validate the design of the TPC and it is expected to give its recommendations by the middle of 2020.

2.2.5 GAS SYSTEM

Within the ND280 upgrade project, it is planned to build a new gas system that will serve both, the new TPCs and the existing ones. We will keep the same gas mixture, Ar-CF₄-iC₄H₁₀ (95:3:2) with a flow rate that will allow 1 volume change per 6 hours and with a fresh injection of gas of 10% in the circulation flow.

The new gas system modules will be designed based on CERN standard and profiting of the CERN experience with gas system from the LHC experiments. The gas system will be running on a Programmable Logic Controller and it will be controlled/monitored using the standard WinCC-OA SCADA interface.

2.2.6 TPC ELECTRONICS

The TPC electronics will be based on the use of the AFTER chips, that had been designed for the existing ND280 TPCs. The AFTER chip is a 72-channel device that includes preamplifiers and shapers with programmable gain and shaping time coupled to a 511-time bucket switched capacitor array (SCA).

8 AFTER chips will be mounted on the Front-End Cards (FEC), that will be installed parallel to the ERAM modules. Each ERAM module will be read by two FECs for a total of 64 FECs for the two HA-TPC. The two FECs on each ERAM will be connected to a Front-End Mezzanine (FEM) card that performs the control, synchronization and data aggregation of the two FECs of a detector module.

As Back-end electronics we will use the TDCM, a generic clock, trigger distributor and data aggregator module designed for several projects, including the upgrade of T2K.

In the last six months we have produced the first prototypes of the FECs and of the FEMs (see Fig. 19). These prototypes have been already tested together. The communication between the two cards was established and it was possible to acquire the pedestals from each channel. The pedestals have the expected values and the next step will be to test the new cards on the TPC prototype at CERN.

2.2.7 NEXT STEPS

One of the critical steps for the HA-TPC project is the beginning of the production by CERN/EP-DT-EF PCB manufacturing facility of the ERAM detector. We expect to produce 3 ERAM detectors per month, thus needing ~ 15 months for the production and qualification of the required 32 ERAM modules.

The first ERAM modules and the electronics will be installed at CERN on the first half of the TPC field cage that will be delivered by NEXUS in September 2020 where cosmics tests will be done.

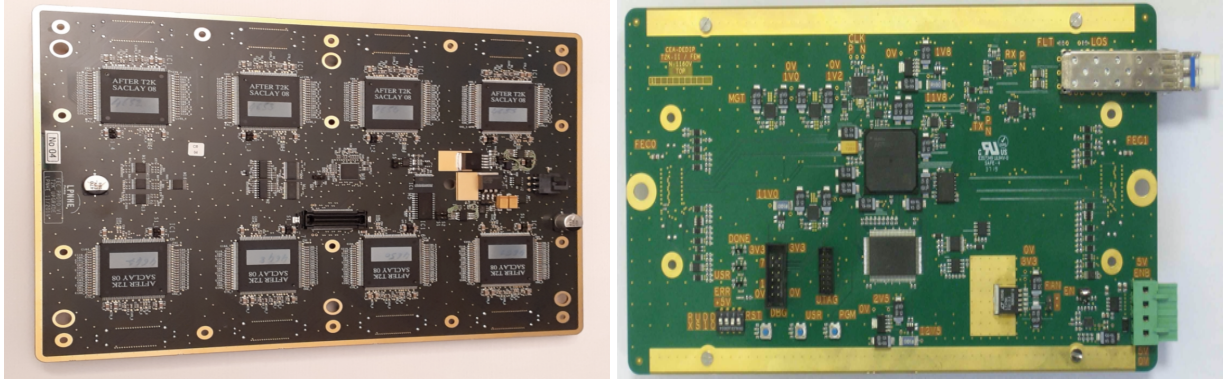


Figure 19: The first FEC (left) and FEM (right) prototypes.

In addition, another test beam campaign has been scheduled at DESY in October 2020 and will allow to test, with electron beam and magnetic field, a final ERAM module on the TPC field cage prototype.

2.3 The Time Of Flight detector

The ToF system will be used to veto particle originated outside of the Super-FGD target. It will also improve particle identification and will provide a cosmic trigger for calibration of detectors which are enclosed inside. Each ToF module is composed by an array of 20 plastic scintillator bars which are stacked in a plane. The total area of one module is $2262 \times 2495 \text{ mm}^2$ (size of aluminum frame). The size of each bar is $2200 \times 120 \times 10 \text{ mm}^3$. The material is a plastic scintillator EJ-200. The bars are wrapped in aluminium foils and a black polyethylene stretch film on top to ensure opacity.

The current status is that all the scintillator bars, the MPPCs, the amplifiers boards, etc. have been procured and the bars have been wrapped and are ready to be assembled into the 6 ToF planes. A photo of one ToF module on the assembly table is shown in Fig. 20 (top-left). After the assembly is completed, we will start the tests with cosmics for the commissioning of the electronics and the calibration.

It is foreseen that for these tests the ToF planes will be installed on a baby-basket that is a replica of the ND280 basket and has been already delivered CERN. The setup will also be used to test with cosmics the HA-TPC and the Super-FGD when they will be ready.

The experimental setup for the cosmic ray measurements is shown in Fig. 20 (top-right). The trigger was formed by the coincidence of signals from two scintillator counters installed on top and bottom with respect to the bar under test. The mean value of the times registered by both beam counters was considered as a reference and was subtracted from measurements of the main bar.

The dependence of the measured time versus position of the crossing point along the bar as viewed by both MPPC arrays is shown in Fig. 20 (bottom-left). The graphs are approximated by linear functions whose slopes represent the effective average speed of light along the bar, which is found to be $v_{eff} = 15.9 \text{ cm/ns}$. One can convert this value into the effective average reflection angle using the refraction index of the plastic, which gives $\theta_{eff} = 33.1^\circ$.

The time resolution of the counter as registered by the arrays is shown in Fig. 20 (bottom-right). The individual resolution evolves from 130 ps for the crossing point near the sensor to 280 ps for the light propagation along the 2 m distance. This deterioration in accuracy is due to the absorption of photons and smearing of the signal leading edge during its propagation. An improvement of the resolution is observed in case of the crossing point being at the proximity of the far end. This could possibly be an effect of light reflected backwards. The resolution of the mean time and the weighted mean measurements is also shown. In both cases the time resolution is approximately 140 ps for the full length of the bar. However the weighted mean approach provides a visible advantage for interactions taking place in vicinity of the sensors.

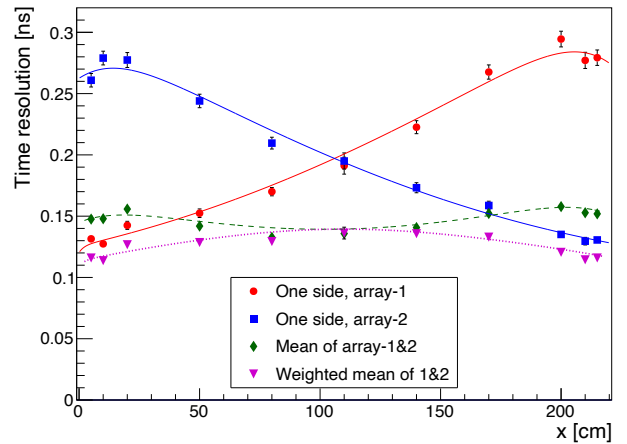
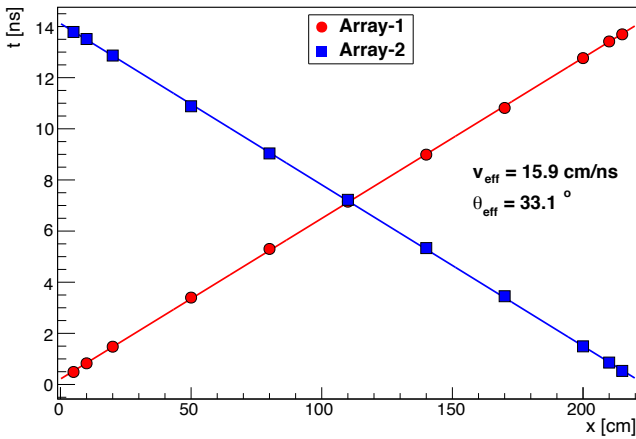
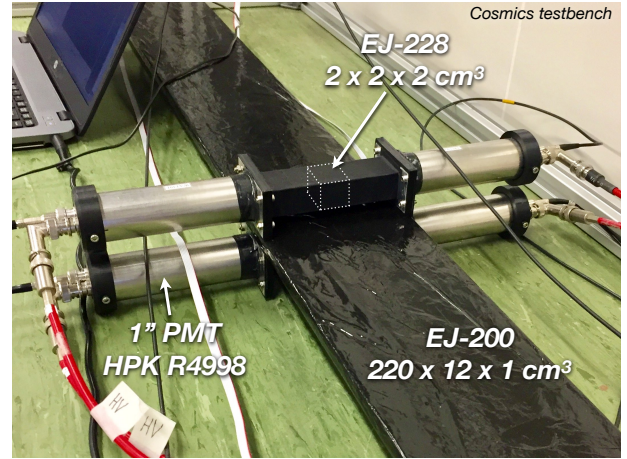
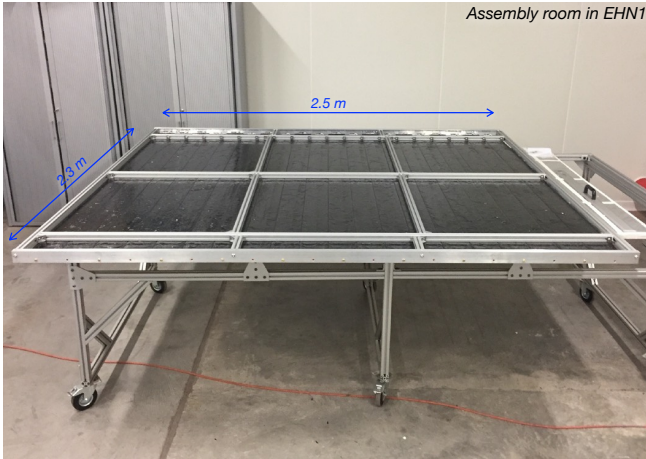


Figure 20: *Top-left*: one ToF module on the assembly table in EHN1. *Top-right*: photo of experimental setup for the cosmic ray measurements. *Bottom-left*: time detected by MPPC arrays at two ends of bar as a function of the trigger position along the bar. *Bottom-right*: time resolution obtained with two MPPC arrays, the resolution of their mean and weighted mean as a function of the trigger position along the bar.

2.3.1 NEXT STEPS

Only a single ToF module has been assembled so far. The mechanical assembly of other five modules will take 1 - 1.5 months. It will be followed by two weeks of tests for the light collection system when amplifiers of every single module will be powered simultaneously and respond to cosmic muons will be reordered. In the meantime, signal cables and patch panels for each module will be produced. Work on the DAQ and slow control systems will begin afterwards.

2.4 Detector Installation

Based on the recommendations from the first review, some modifications to the installation procedure were decided. In a first step, the detector envelopes for each subdetector were defined and documented in an internal technical note.

The installation procedure was adapted and worked out as following:

1. Removal of the POD including the upstream ECAL. Originally we had considered to leave it in place.

2. The insertion is started with the downstream TOF panel, which is located between the new sub-detectors and the first vertical TPC from the current tracker system.
3. Then the bottom TOF panel will be installed.
4. This is followed by the installation of the bottom TPC.
5. After the commissioning of the bottom TPC in the basket, the SuperFGD will be inserted. Since the electronics crates when connected to the SuperFGD box will exceed the space available within the basket, the insertion will be done with the box alone and then the electronics crates will be installed from the sides. The full system will be commissioned before the next installation step.
6. The installation will be continued with the insertion of the top TPC.
7. This is followed by the re-installation of the upstream ECAL and the insertion of the upstream TOF panel.
8. As last step, the side TOF panels will be installed.

To test the fixation and the insertion of the different subdetectors, Franck Cadoux from the University of Geneva designed a mock-up of the basket section corresponding to the POD position. This mock-up is already produced and available at EHN1 at CERN (Fig. 21).

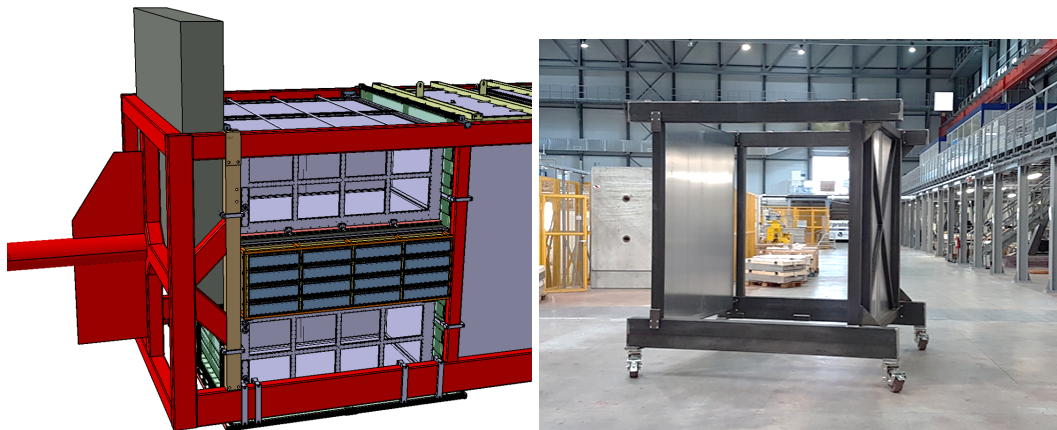


Figure 21: *Left:* CAD sketch of the basket during the ECAL re-installation. *Right:* Photo of the BabyBasket which reassembles the same geometry as the ND280 basket.

2.5 Project Time Schedule

We have updated the project timeline taking into account known delays due to COVID-19 and other effects as shown below. With this new schedule, the installation of the detectors in the basket are foreseen in Summer 2022. The new detectors will be ready for beam by fall 2022.

Super-FGD

- 03/2021:** All cubes assembled in x-y layers
- 06/2021:** Finishing assembly of 6 TOF panels at CERN
- 08/2021:** Assembly of layers in the box
- 10/2021:** Super-FGD shipped to J-PARC
- 12/2021:** Insertion of WLS fibers
- 02/2022:** Installation of MPPC and calibration system

03/2022: Installation of Super-FGD electronics

04/2022: Tests on surface at J-PARC

04/2022: Ready for installation in the basket

HA-TPC

12/2020: Delivery of first half of field cage to CERN

02/2021: 8 ERAM modules and FE electronics

06/2021: Design and construction of gas system at CERN

08/2021: First TPC fully instrumented

10/2021: Cosmic tests at CERN with full first HA-TPC

12/2021: First TPC ready for shipment

12/2021: Infrastructure for gas system at J-PARC

04/2022: Second TPC instrumented and ready for shipment

Integration at J-PARC

By 03/2022: POD removal and basket modification

03/2022: Installation of bottom TOF panel

04/2022: Installation and commissioning of bottom HA-TPC

05/2022: Installation of Super-FGD

06/2022: Commissioning of Super-FGD

07/2022: Installation and commissioning of top HA-TPC

07/2022: Installation of upstream POD and TOF panel

08/2022: Installation of remaining TOF panels

3 Super-FGD Assembly method

Two different methods have been investigated for the assembly of the cubes into the final Super-FGD detector: the fishing-line and ultrasonic welding methods. The former method utilizes fishing-lines with 1.3 mm diameters which are inserted into the cube holes (1.5 mm diameter) to keep the fiber hole alignment. The assembly procedures consist of forming layers of 192×184 cubes by connecting 184 strings of 192 cubes with fishing lines and merging the layers into the Super-FGD volume. The alternative method uses ultrasonic welding to assemble cubes between two thin sheets with controlled pitches. The welding machine provides a sheet module which consists of an array of 32×24 cubes; a vertical slice of full detector (plane module) consists of 14 sheet modules and a full detector consists of 176 plane modules. This method has the advantage of providing a rigid structure with fixed cube position; however, it requires better quality control of the single cubes and brings additional dead materials to hold the layers inside the mechanical box.

An external review committee has been formed by the T2K Executive Committee to review the feasibility of the two assembly methods in November 2019. In this review, the fishing line method was recommended as the baseline option with the recommendations given below:

The baseline fishing line method has been well prototyped and is currently being implemented with a significant proportion of layers already assembled with fibre optic cables. This gives confidence that resources that are currently being utilized should be sufficient to complete the full assembly on schedule. The main outstanding question for this method relates to the seismic stability.

The backup ultrasonic welding method offers greater structural integrity (which could be enhanced further) and should be less labour intensive than the fishing line method. However this method requires more infrastructure development particularly for the QA. In addition the WLS fibre installation takes place at the end of the installation so any severe hole misalignment (due to a failure of the QA) would be difficult to recover from.

Following the recommendation, we decided to concentrate all the efforts on the fishing-line method; the developments of the ultrasonic welding method have been halted.

3.1 Fishing Line Method

The main concept of the fishing line method is to ensure the alignment of the cube hole positions with the plastic threads. A fishing line of 1.3 mm diameter is used to build arrays of 192 cubes, which the arrays are then connected to each other by the fishing lines to form layer of 192×184 cubes. The fishing lines hold layers of cubes together in the position to form volume of Super-FGD, and it provides accurate positioning of WLS fibers for the correct coupling to photo-sensors attached to the mechanical box during the assembly.

3.2 Cube Array Assembly

The cubes undergo quality inspection using 1.4 mm diameter metallic needle to reject cubes with misaligned holes or nonuniform cubes. This cube quality inspection is done in a plane of $14 \times 14 = 196$ cubes by threading metallic needles through the horizontal holes. The plane is visually inspected for flatness, gaps between the cubes, and structural uniformity to identify the faulty cubes. Few percents of faulty cubes are found in the full inspection, which are replaced by other cubes to re-do the inspection. The assembled plane is shown in Figure 22.

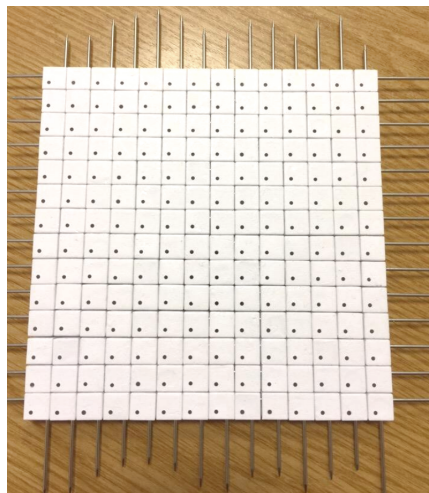


Figure 22: 196-cubes array for the quality inspection.

The vertical holes of the plane are then inspected. All the needles are extracted from one side of the plane to turn each cube row by 90 degrees. All the needles then put back through the horizontal holes to check the hole alignment with the visual inspection.

Once the plane completes the inspections, 4 cubes are removed from the plane to form an array of 192 cubes. The needles are extracted channel by channel to thread a 2.2 m long fishing line through the cubes row by row until it forms the array. The threading procedures are shown in Figure 23, and the assembled cube arrays are shown in Figure 24.

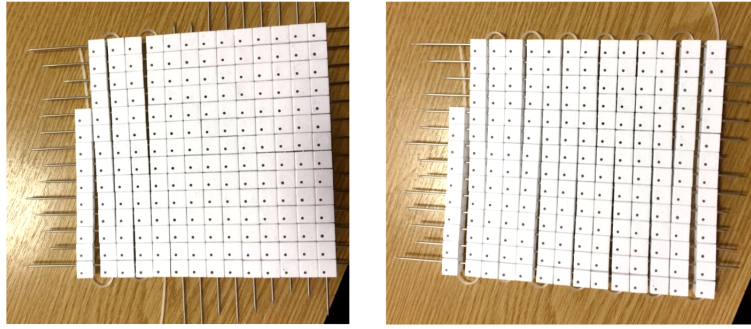


Figure 23: Threading the fishing line through 192 cube array.



Figure 24: Picture of assembled 192-cube arrays with fishing lines.

3.3 Cube Layer Assembly

The layer of Super-FGD detector is assembled by merging 184 cube arrays with fishing lines. In order to facilitate the layer assembly, two 92 cube arrays are merged independently to form two half-planes. In each part, the orientation of holes and position of the cubes are fixed with 1 m long, 1.2 mm diameter spokes as shown in Figure 25. The spokes are inserted perpendicular to the fishing line direction in each cube row to keep the position fixed.



Figure 25: The layer assembly by dividing the cube arrays in two half-planes. Each divided layers consist of 92 cube arrays, and the arrays are aligned by the 1 m long, 1.2 mm diameter spokes inserted through the horizontal holes.

Then, the two half-planes are aligned to each other to merge into single, 192×184 Super-FGD array. The spokes the replaced channel by channel with the fishing lines; the fishing line is threaded through each row of 184 cubes with rotations. If the fishing line does not pass through the fiber hole smoothly,

the hole alignment of the cube arrays are investigated by shifting the position the cube array where it got "stuck". In addition, there is a possibility that the diameter of the fishing line exceeds the specified value of 1.3 mm; the fishing line is replaced by the new one in this case. During this assembly procedure, the fishing line ends are trimmed in advance to have semicircular shape to allow smooth insertion through 184 cube arrays.

3.4 Super-FGD Volume Assembly Test using Prototypes

The volume assembly requires alignment of 192×184 fiber holes along 56 layers of 192×184 Super-FGD cubes. In order to investigate and optimize the volume assembly procedures, two Super-FGD prototypes are assembled and tested for the feasibility. The first prototype consists of $192 \times 5 \times 184$ Super-FGD cubes, which is named Plane Prototype. 5 192×184 planes were mounted and aligned by the right angle aluminum profile as shown in Figure 26). The vertical matching of holes is checked by inserting 1.4 mm diameter needles which were used in the cube array quality check.



Figure 26: The $192 \times 5 \times 184$ Plane Prototype assembly using the right angle, aluminum profile. The height of the corner is equivalent to 5 Super-FGD cubes.

The needles are inserted vertically with pitch of approximately one needle per 40 cm^2 over the Super-FGD planes to fix the fiber hole positions as shown in Figure 27). The remaining five vertical channels are checked with the needles for the vertical alignments. The needles can be inserted smoothly through the tested channels.

A second, $15 \times 56 \times 192$ -cube prototype, named Wall Prototype, is used to test the feasibility of the vertical channel alignment with the full-size Super-FGD detector height. As shown in Figure 28, the Wall Prototype is mounted on the Plane Prototype in the initial assembly tests.

The Wall Prototype is assembled by repetitively merging a batch of 5-6 15×192 narrow layers. Once a batch of narrow layers are placed, they are aligned vertically by inserting 1.4 mm diameter needles through the vertical holes in few centimeters pitch. Once the layers are aligned properly, the needles were removed to merged an another batch. At the end, 56 layers were placed and held by replacing the needles with 1.2 mm diameter, 1 m long spokes through the vertical holes in few centimeter pitch.

Few of the 192-cube long, horizontal channels in both Wall and Plane Prototypes undergo the fiber insertion tests. The 1.3 mm diameter fishing lines are removed and replaced by 1 mm diameter WLS fibers as shown in Figure 29. Once the WLS fiber insertion is performed, the fishing lines are replaced back into the Prototypes. The fibers were inserted and removed smoothly in all of the cases.

3.5 Fiber Insertion Test with Controlled Detector Sagging

The Wall Prototype was dismantled from the Plane Prototype to perform the fiber insertion tests with detector sagging. The test is performed by setting the Wall Prototype on different support stands to

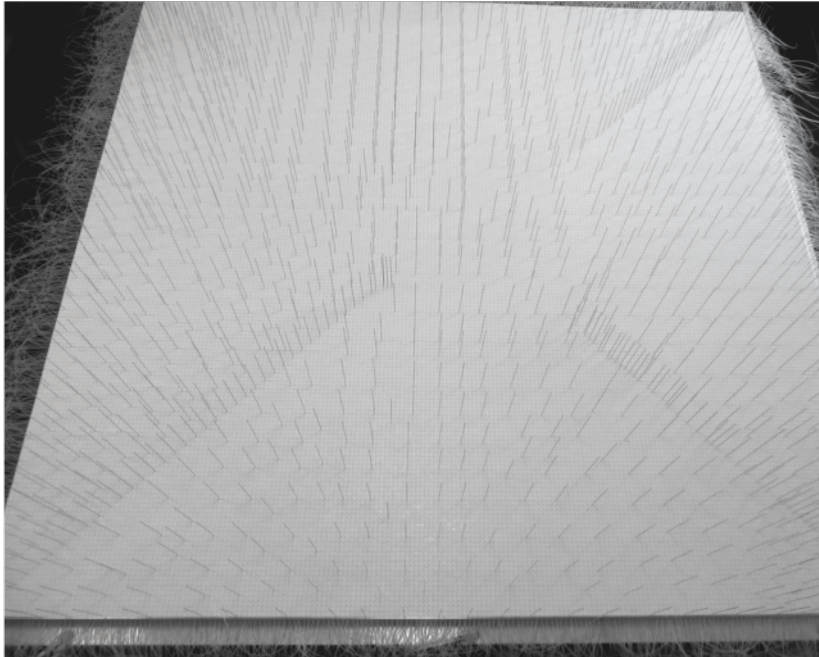


Figure 27: Merging the 5 cube planes with the 1.4 mm diameter needles.



Figure 28: Picture of both Wall ($15 \times 56 \times 192$ cubes) and Plane ($192 \times 5 \times 186$ cubes) Prototypes assembled with fishing lines.

intentionally introduce up to 20 mm sagging depth at the center of the Prototype¹. The sagging depth is defined as the perpendicular distance from the middle of the top cube layer to the straight line between both layer ends. The purpose of the test is to check how the fiber insertion will be affected at the different sagging depth. The picture of the sagging test setup is shown in Figure 30.

During this test, 1 mm diameter fishing lines are inserted in the vertical channels to imitate the WLS fibers. The regular, 1.3 mm diameter fishing lines are kept in the horizontal channels unless they are replaced by the WLS fibers for the fiber insertion tests. The deflection of the bottom plate is maintained with a few support points to obtain the symmetrical parabola with a specified sag values.

In each test with different sagging depth, the 1.3 mm fishing lines are removed from some of the 192-cube long channels at the lowest level of the layers. 2.2 m long 1 mm diameter WLS fibers are inserted in those channels to check the effect of the sagging depth to the fiber insertion. The fiber ends are not specially treated in this test. As shown in Figure 31, the fiber insertion is performed

¹Note that the maximum sagging expected for the full detector is 3–4 mm.

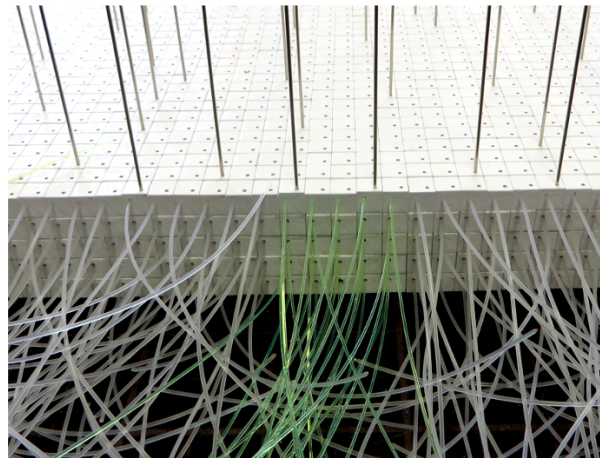


Figure 29: Picture of WLS fiber insertion in 192-cube long, horizontal channels in the Plane Prototype.

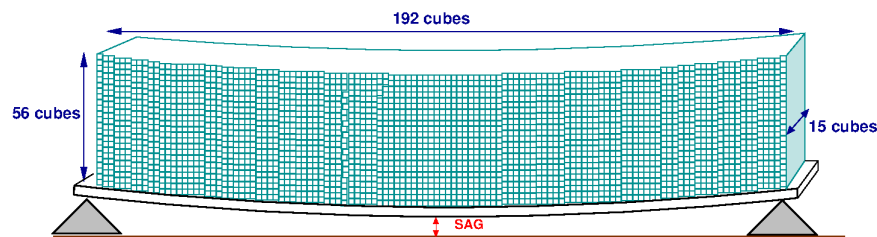


Figure 30: Picture of the sagging test setup.

without observing the effect of clamping. Once the fiber insertion is performed and inspected, the WLS fibers are replaced by the 1.3 mm fishing lines. The same procedure was repeated at the fifth plane from the bottom; similar to the previous tests, no effect of friction is observed during the fiber insertion. However, during the test with 20 mm sag depth, difficulty of the fishing line re-insertion is



Figure 31: Wall Prototype with sagging depth of 10 mm. Inserted picture shows the WLS fibers inserted in the lowest layer of the Prototype.

once observed. In this case, the fishing line was needed to be inserted from the opposite end of the channel. No additional equipment such as spokes for channel cleaning is needed during this fishing line re-insertion. In addition, the mobility of fishing lines along the 192-cube long, horizontal channels is tested with sagging depth of 20 mm. The 20 mm sagging is demonstrated in two setups: a support stand and the panel that is used for the mechanical box. Approximately a hundred fishing lines along 15×56 channels are moved in and out within a range between 5 to 10 cm by fingers with the support

stand setup, while all 840 fishing lines are tested with the panel setup. The checks confirmed that the fishing lines can be moved without using any tools or experiencing any clamping inside the Super-FGD cubes. With the panel setup, about 30 random fishing lines were removed completely and 2 m long WLS fibers were inserted instead. The fiber ends were cut under 90 degree, without any other special treatment. All fibers were installed and removed smoothly. Careful installation takes about 2 minutes per a fiber in average. Then, all fishing lines were pushed back in place without any problem as well.

3.6 Full-size Super-FGD Assembly

The full-size assembly of Super-FGD inside the mechanical box require a mounting table and a movable platform to keep a person above the mounting table. The platform provides worker's access to the top surface of the detector. The conceptual drawing of the table and platform is shown in Figure 32. Three adjacent sides of the mechanical box are placed on the mounting table to align the Super-FGD fiber holes with the mechanical box. We expect the mounting table to elevate the box by pillars to provide accessibility to each side of the mechanical box.

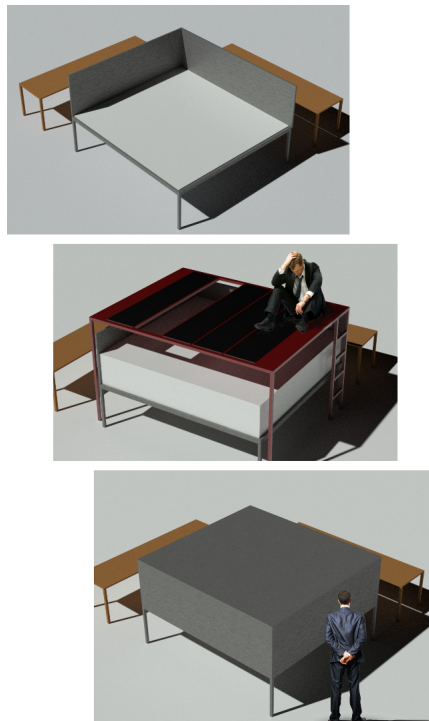


Figure 32: Conceptual approach to assemble Super-FGD inside the mechanical box.

The first layer is placed and adjusted into the box with fishing lines by pulling them through the box side wall. The layer is then fixed to the box bottom wall with 1.4 mm diameter needles. We expect the needles to be placed every 30-40 holes to align the cube fiber holes to perform smooth insertion of the fishing line. All successive layers will be merged with the vertical holes of the first layer. The assembly proceeds by merging layers one by one, by following the same procedure as the one for the narrow-size prototype. As it was demonstrated in the prototype assembly, we expect the assembly can be carried out by merging batches of multiple layers; details of the procedures must be verified during the full-size assembly. When more than 20 layers are merged, the further merging is performed with both 1.4 mm diameter needles and longer, 1.2 mm diameter spokes.

After 56 planes are assembled, the remained box surfaces are installed to close the mechanical box. All of the vertical spokes are once removed from the top surface, and then some of them are re-inserted from the bottom of the box. Once the surface of the box is installed, rest of the vertical spokes are inserted back from the top of the box. Rest of the side walls are installed; during this process, the

fishing lines are pulled out from the fiber holes of the side wall to keep the alignment of the cube holes. Once the mechanical box is closed, the spokes and fishing lines are replaced with WLS fibers to complete the Super-FGD assembly.

3.7 Super-FGD Assembly Time Line

Assembling the cube planes is going on jointly with the cube production process. As a shipment of the cubes is delivered to INR RAS, Moscow, the cubes are embedded in the plane before the next delivery occurs. With the stable cube production rate, we expect the assembly rate of one 192×186 -cube plane per week.

Two shipments of the cube planes from INR to CERN are planned to facilitate the assembly inside the mechanical box. First batch of about 30 planes was planned to be shipped by May, 2020; however, due to the COVID-19 quarantine situation the delivery is delayed to Fall 2020. The second shipment with the remaining planes is expected to be done in March-April, 2021. The first delivery allows to start the assembly process upon the readiness of the mechanical box. The planes will be packed in 2.1×2.1 m² boxes and delivered to CERN by trucks. Once the whole cube planes are assembled inside the mechanical box, the box will be closed with the fishing lines left to be shipped to J-PARC in May, 2021, for the replacement of fishing-lines with the WLS fibers.

A conservative estimation of the required time to merge all 56 planes to the mechanical box is approximately 30-36 working days of uninterrupted work. The estimation is made with an assumption of two shifts in a day, four persons in each shift. We expect a single plane to be merged per shift, which results the merging of two planes per day. Minimum of four persons are required to transfer and handle a cube plane. With the four person shift, the mechanical box closure and the WLS fibers replacement are expected to take about 30 working days total.

3.8 Ultrasonic Welding Assembly Method

Ultrasonic welding method is investigated as an alternative for the Super-FGD assembly. The key concept of this method is to ensure the controlled clearance between the cubes by fixing all cubes at right and settled positions on the polystyrene sheet. With this assembly method, we expect no shearing stress to the fibers due to cube displacement induced by vibration during and after the assembly.

The cubes are attached to the polystyrene sheet in an array of 32×24 cubes to form a sheet module with a technique called ultrasonic welding. This method utilizes ultrasonic vibration to join thermoplastics by "welding" the pieces together. In this assembly method, no gluing material, which can cause the degradation of scintillator materials and additional size variation, is used. A jig is used to providing fixed, precise pitches between the cubes for the WLS fiber insertion.

The cubes are fixed between two thin sheets with controlled pitches, which allow the smooth WLS fiber insertion by providing a clearances for the cube size variation. A plane module is made from 14 sheet modules to provide vertical slice for the full detector (192×56 cubes). Finally, 176 plane modules are integrated in the mechanical box. Total of 2,464 sheet modules are necessary to build full detector. A conceptual drawing of the module production with the ultrasonic welding is shown in Figure 33. Since the modules form vertical slice of the detector, two polystyrene bars are attached to the plane module to support it at stood placement during the module integration into the mechanical box.

Similar to the fishing line method, we expect to use the mounting table for the full-size detector assembly with the ultrasonic welding method. The procedures of the plane module integration to the mechanical box is shown in Figure 34. The plane module is transported into the box by a rigid long bars passed through the polystyrene bars. Once the plane module is placed in the box and aligned with the two bottom corners, the plane module is fixed by 4 pins at the holes of plastic bar attached to the plane module. This procedures are repeated until the full module integration; its alignment along Z axis is checked for each module integration. The mechanical box is closed once the modules are fully integrated; the fiber insertion follows after the box closure.

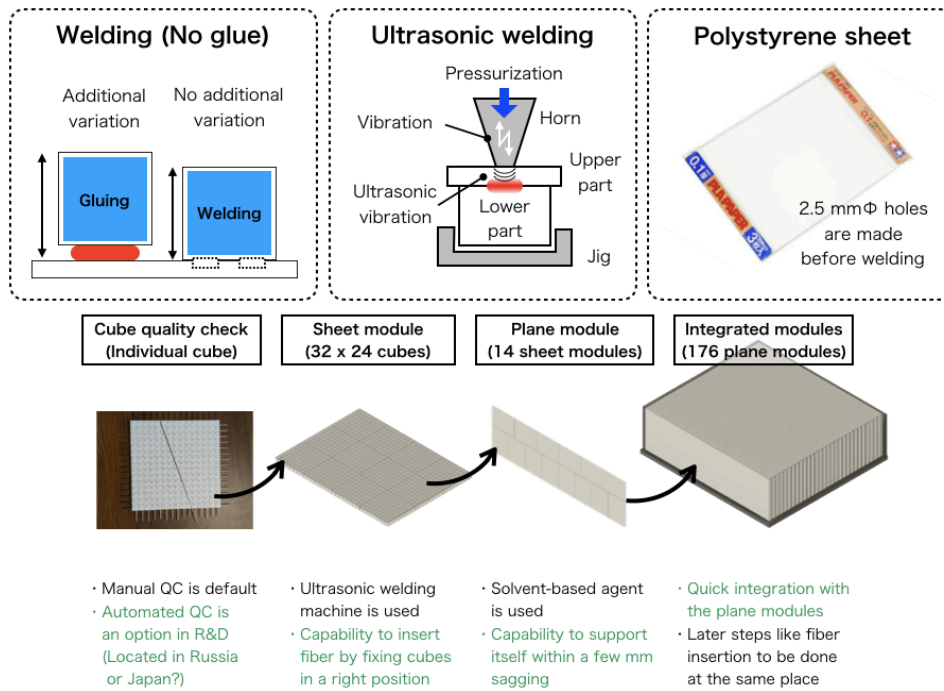


Figure 33: Conceptual drawing of Super-FGD assembly with the ultrasonic welding method.

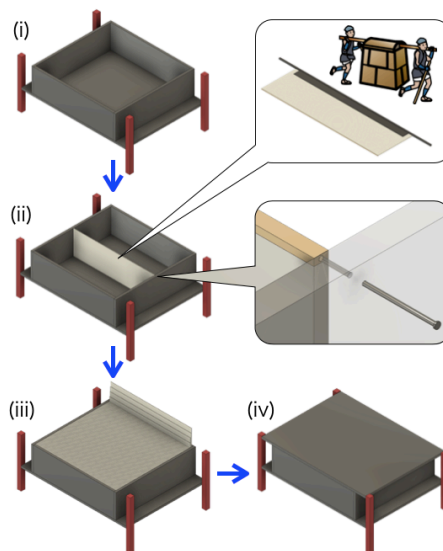


Figure 34: Assembly of the all modules.

The fiber insertion test demonstrated that the precise cube quality check is critical for the ultrasonic welding method. A prototype which consists of 5 sheet module is used to perform fiber insertion test with two configurations of dimension: $32 \times 5 \times 24$ and $160 \times 1 \times 24$. Scintillator cubes used in this test are produced in the early phase before the production precision optimization; as a result, while fibers can be inserted for most of the channels, there are some channels which failed the fiber insertion. An another test was performed with the cubes produced after the precision improvement. Since an amount of such cubes are limited for this test, three lines with 184 cubes per line aligned with a jig to imitate the welding assembly; it was confirmed that the fibers can be inserted smoothly in this configuration.

The basic feasibility of the ultrasonic welding method was demonstrated with sheet modules. However, this method still requires more development of the plane module assembly and QA/QC to establish a robust assembly procedure. Considering the limitation of available resource and time, we decided to focus the efforts on the fishing-line method.

4 Sensitivity studies

Detailed description of the expected performances of the ND280 Upgrade can be found in [1]. In this section the main results will be recalled and more recent studies will be introduced. These additional studies show the high potential of the ND280 upgrade to improve the current knowledge of neutrino-nucleus scattering models, thanks to its excellent capabilities in reconstructing both, the leptonic and the hadronic part of the neutrino and antineutrino interactions.

In Fig. 2 we showed the selection efficiency for Charged-Current (CC) inclusive ν_μ events in neutrino enhanced mode as a function of the muon angle with respect to the neutrino beam direction and the reconstruction efficiency for protons as a function of their momentum. The upgraded ND280 drastically improves the acceptance for muons produced at high angles as well protons of low momenta. These better efficiencies have an impact on the constraints of ND280 to the oscillation analyses. In ND280 Upgrade we expect to select $\sim 100 k$ charged-current neutrino interactions in the Super-FGD per 10^{21} p.o.t.. These numbers are obtained by requiring that the muons issued by the neutrino interactions are reconstructed also in the TPC.

The ND280 fit used for the T2K oscillation analyses, was performed by using the Current and the Upgrade configuration, assuming the statistics of 8×10^{21} p.o.t.. A comparison of the post-fit errors of some of the most significant systematic parameters are shown in Table 1. On average the error on the systematic parameters is reduced by about 30%. Further improvements are expected by including muons stopping in the Super-FGD that would add 15% of events, mostly in a phase space only partially covered by the ND280 Upgrade if reconstructed tracks in the TPC are required. In addition, no attempts to select exclusive samples with reconstructed protons have been done for these studies.

Table 1: Sensitivity to some flux and cross-section parameters of interest for the current ND280 and the upgrade configuration with $f 8 \times 10^{21}$ POT.

Parameter	Current ND280 (%)	Upgrade ND280 (%)
SK flux normalisation ($0.6 < E_\nu < 0.7$ GeV)	3.1	2.4
MA_{QE} (GeV/c ²)	2.6	1.8
ν_μ 2p2h normalisation	9.5	5.9
2p2h shape on Carbon	15.6	9.4
MA_{RES} (GeV/c ²)	1.8	1.2
Final State Interaction (π absorption)	6.5	3.4

In Fig. 35 the main post-fit systematic errors are shown. The ND280 upgrade can provide overall smaller systematic uncertainties to the oscillation analysis.

The uncertainty on the total number of events selected at the T2K far detector, Super-Kamiokande (SK), was evaluated using the best-fit ND280 covariance matrix obtained by the Asimov data set fit in the upgrade configuration and are shown in Tab. 2. The neutrino cross-section parameters that cannot yet be constrained by the ND280 detector, like $\sigma_{\nu_e}/\sigma_{\nu_\mu}$ ratio and the NC parameters, are not propagated from ND280 to SK analysis.

Table 2: Sensitivity to some flux and cross-section parameters of interest for the current ND280 and the upgrade configuration.

Source of uncertainty	ν_e CCQE-like $\delta N/N$ (%)	ν_μ $\delta N/N$ (%)	ν_e CC1 π^+ $\delta N/N$ (%)
Flux + cross-section (constrained by ND280)	1.8	1.9	1.4

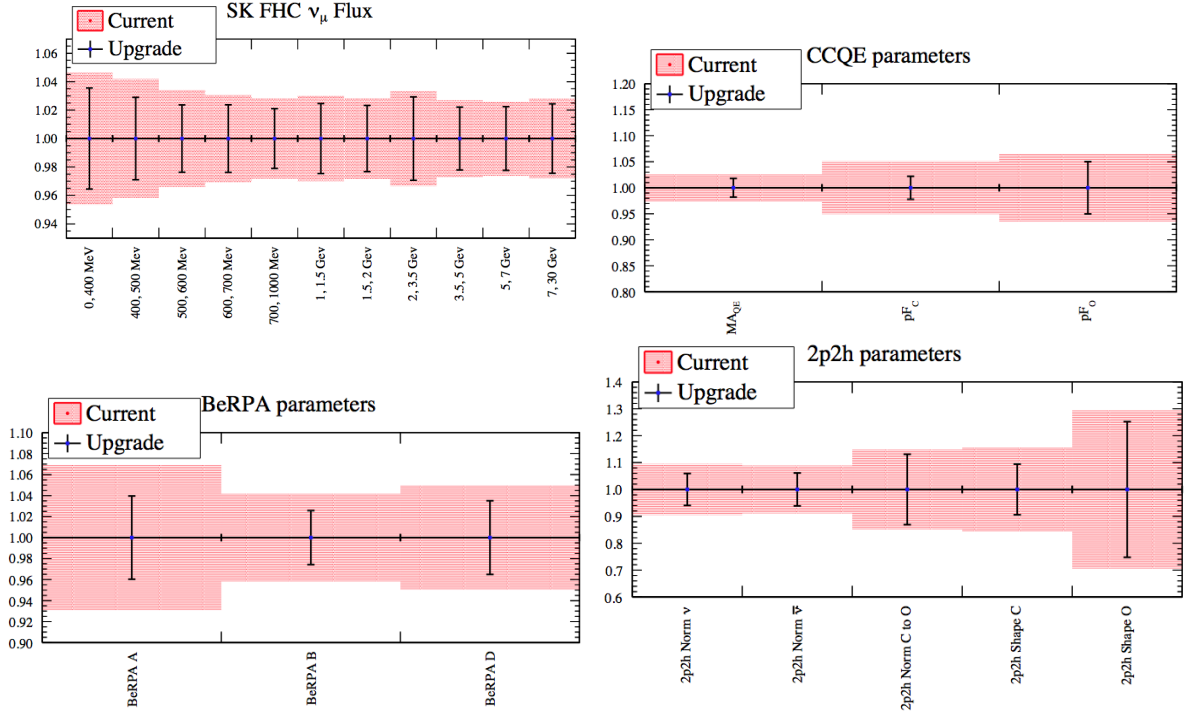


Figure 35: The post-fit errors on the main systematic parameters are shown for both the ND280 upgrade (blue dots) and the current ND280 configuration (red bars). These sets of parameters comprise the far detector ν_μ flux (top left), the CCQE cross-section (top right), the Random Phase Approximation (bottom left) and 2p2h parameters (bottom right).

4.1 Prospects for the T2K oscillation analysis

In order to estimate the impact of the ND280 upgrade over the future neutrino oscillation measurements of T2K, a reasonable estimate on the extrapolation at high statistics of the present uncertainties, quoted for instance in Ref. [3], can be done.

The ND280 unconstrained cross-section uncertainties, notably on the number of ν_e events, are dominated in Ref. [3] by the effect of the binding energy. This is the energy needed to extract a nucleon from the nucleus in a neutrino-nucleus interaction. This quantity has been actually measured with good precision in electron scattering data and it is expected to be the same in electron-nucleus and neutrino-nucleus interactions (see, for instance, [4]). Unfortunately the electron scattering constraints could not be included in the neutrino interaction model used in Ref. [3] due to time constraints. Moreover, in that analysis the binding energy uncertainty was not constrained by the ND280 data.

A new model [5], with more careful treatment of binding energy and other nuclear effects, is already implemented in the new version of T2K Monte Carlo. The framework to exploit the ND280 data to constrain the binding energy has also been developed. T2K 2020 results are expected to feature a much reduced uncertainty on the binding energy. Such constraints will be further highly improved by the ND280 upgrade thanks to the new capabilities of Super-FGD to reconstruct low momentum particles and neutrons. In the next section the improvement on neutrino energy reconstruction and the corresponding very good precision on binding energy are quantified. Moreover, high statistics sample with low muon momentum can be selected in the Super-FGD standalone. Figure 36 shows the muon momentum spectrum for events reconstructed and selected following neutrino interactions in the FGDs and the Super-FGD: the power of the latter is clearly visible enabling larger statistics, notably in the low momentum region where the effect of binding energy is particularly relevant. The Super-FGD low threshold for muons and protons, complemented by the mentioned improvements in the model, will allow to constrain the binding energy uncertainty well below the other systematic uncertainties.

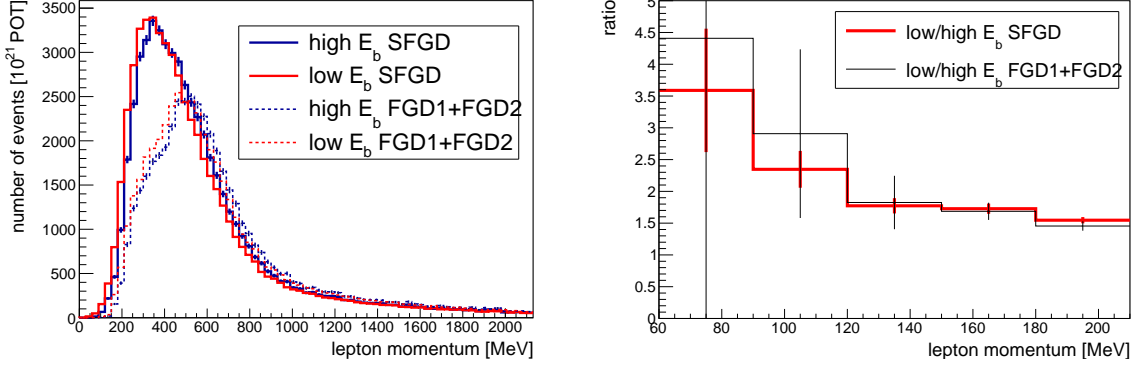


Figure 36: Left: spectrum of muon momentum with different binding energy values (16 MeV and 43 MeV), as evaluated in Ref. [3] for CCQE events selected in FGD1 and FGD2 with ND280 detector and in Super-FGD with ND280 upgrade detector. Right: ratio of the spectra with different binding energy. Statistical errors only.

In T2K-II the dominant ND280 unconstrained cross-section uncertainty will be due to the difference between ν_e and ν_μ interactions. ND280 upgrade will feature a more precise ν_e cross-section measurement with respect to ND280 [6], thanks to the better purity due to the expected improved electron/ γ separation in the Super-FGD. Nevertheless, due to the purity of the T2K ν_μ beam, the ν_e sample will have too low statistics to enable a few % precision, thus the ν_e/ν_μ uncertainty will be mostly driven by theoretical considerations. The impact of secondary class current and radiative corrections [7], which depends on the mass of the outgoing lepton, should be calculated and included in the models. A more precise measurement of nuclear effects in ν_μ interactions will also help in reducing the ν_e/ν_μ uncertainty, as shown for instance in [8] and discussed in Sec. 4.2.3.

The systematic uncertainties related to the SuperKamiokande detector are estimated using a sample of atmospheric neutrinos and are today conservatively treated and limited by the available statistics. The reduction of the other systematic uncertainties and the larger statistics of atmospheric neutrinos will call for a refinement the evaluation of systematic uncertainties. Possible improvements would consist in finer bin of the kinematic variables used to parametrize the uncertainties and avoiding double counting with the cross-section uncertainties in the T2K analysis. No official estimate is available yet, but we can reasonably evaluate these uncertainties at high statistics to be well below the present 2%.

Finally the uncertainties due to Final State Interactions (FSI), Secondary Interactions (SI) and Photo-Nuclear (PN) effects are today conservatively quoted to be around 2-3%. The PN effects corresponds to the emission of low-energy photons from the excited nucleus following the neutrino interactions. This process may induce some NC background events to be misidentified as 1-Ring ν_e events but this effect is sub-dominant with respect to FSI and SI uncertainties. In the present T2K analysis the constraints on the FSI and SI from the near detector are not propagated to the far detector, because of lack of information on the correlation between Carbon and Oxygen uncertainties. This problem has been recently studied in Ref. [9] where a detailed fit to all the pion-nucleus scattering data, including different target materials, is performed and an improved FSI uncertainty is obtained. Moreover recent improvements in the Monte Carlo allowed to describe FSI and SI in the same model and thus improving the constraints on such effects, fully exploiting their correlation. Such developments will be complemented by a high statistics sample of neutrino interactions on Oxygen in the WAGASCI detector [10]. Exploiting these new developments and the expected results on Oxygen, a residual FSI, SI and PN uncertainty of the order of 1% can be considered for T2K-II.

In summary, on the basis of these estimates, the uncertainties on the number of events at SuperKamiokande can be extrapolated for T2K-II to be of the order of 1% (3%) due to ND280 unconstrained ν_μ (ν_e) cross-sections, 1% due to FSI, SI and PN effects and 1% due to the SuperKamiokande

detector. It is therefore crucial to strengthen the ND280 constraints on flux and cross-section uncertainties well below 2%. The analysis shown in the previous section, exploiting only the samples with muons reconstructed in the horizontal and vertical TPCs, have shown that a relative improvement of 30% on such constraints can be obtained thanks to the ND280 upgrade, enabling uncertainties below 2% with 8×10^{21} p.o.t.. The summary of the expected systematic uncertainties is reported in Tab. 3. The expected sensitivity on Charge-Parity violation search for this level of systematics is shown in Fig. 37. This plot shows that the sensitivity of T2K reaches 3σ at 15×10^{21} p.o.t. in total for the maximal CP violation case, and highlights the importance of systematics reduction which is the main aim of the ND280 upgrade.

Table 3: Projected systematic uncertainties for the oscillation analysis in T2K-II. The constraints of ND280 upgrade are evaluated for 8×10^{21} POT. The total is evaluated considering the various sources of uncertainties to be uncorrelated.

Source of uncertainty	ν_e CCQE-like	ν_μ
	$\delta N/N$	$\delta N/N$
ND280 unconstrained cross-section	3%	1%
Flux + cross-section (constrained by ND280 upgrade)	1.8%	1.9%
SuperKamiokande detector systematics	1%	1%
Hadronic re-interactions	1%	1%
Total	3.8	2.6

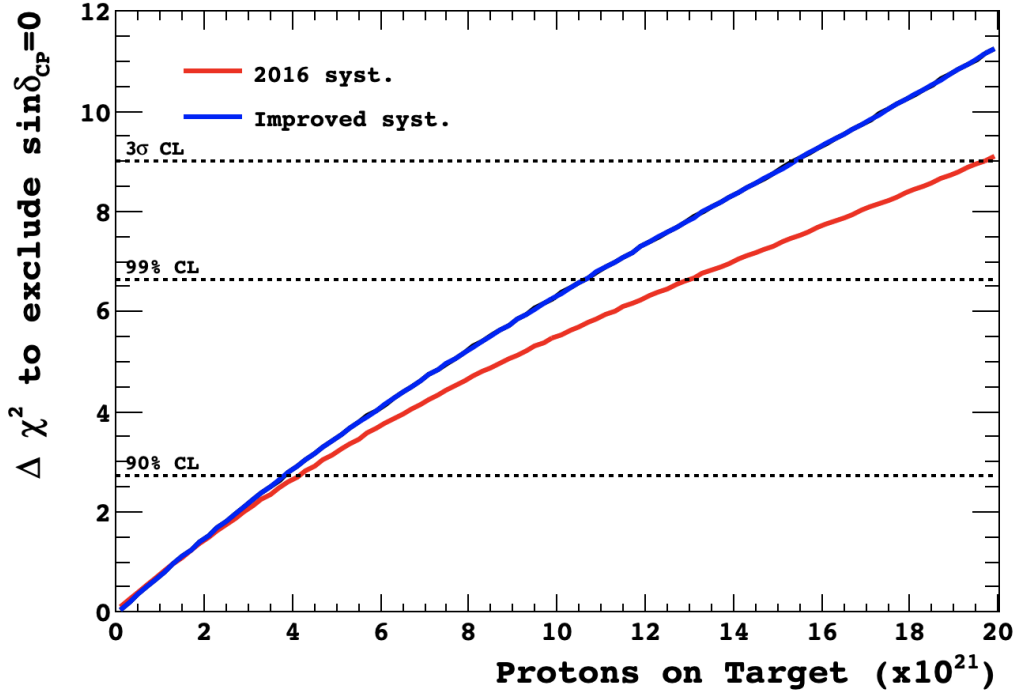


Figure 37: Sensitivity to Charge-Parity violation as a function of POT. The systematic uncertainties corresponding roughly to Ref. [11] are compared to the case of 4% systematic uncertainties on all the SuperKamiokande samples, as can be conservatively estimated in T2K-II using the constraints from ND280 upgrade (see Tab. 3).

4.2 Physics potential with low momentum protons and neutrons

A possible evidence of Charge-Parity violation at 3σ level in the neutrino oscillation will certainly require an unprecedented control of the complex systematic uncertainties due to neutrino-nucleus interaction modeling. The previous results of T2K along the years have shown that the modeling of neutrino-nucleus interactions is a delicate task and, each time the precision of ND280 constraints increases with the statistics, new area of such modeling have been explored and new challenges arise. The new samples of low momentum muons and protons in Super-FGD and the new sample of high angle muons in the HA-TPC will be a crucial input to meet these challenges and to allow a robust estimation of the systematic uncertainties.

In this section we will show how the enhanced capabilities of the Super-FGD in the reconstruction of low momentum protons and in neutron detection will boost the sensitivity of the ND280 upgrade to cross-section models. The full inclusion of such measurements in the oscillation analysis requires the development of a more sophisticated framework, with respect what is used in T2K today. Such work is being carried out by the ND280 Upgrade collaboration in preparation for T2K-II. Here we report preliminary results using a simplified simulation and analysis.

The main limitation in the model-dependent T2K analysis, as of today, is due to the limited capability of constraining nuclear effects by using only the kinematics of the outgoing lepton from neutrino interactions. Examples of relevant nuclear effects which impact the oscillation measurements are the Fermi momentum of the initial nucleon inside the nucleus, the binding energy necessary in order to extract such nucleon from the nucleus and the component of non-QE events without pions in the final states. Such nuclear effects drive the resolution and the scale of the reconstructed neutrino energy at SuperKamiokande (E_{rec}), which needs to be precisely modeled in order to avoid biases in the oscillation measurement. The reconstruction of protons (and neutrons) in the final state allows a direct probe of such nuclear effects, as pioneered by T2K and Minerva cross-section measurements [12, 13, 14]. Single Transverse variables (STVs, a combination of proton and lepton kinematics) have been proposed in Ref. [15] and other variables can be conceived. Here we will discuss, for instance, the reconstructed total momentum of the initial nucleon from the muon/proton kinematics (p_n introduced in Ref. [16]) and the sum of the muon and leading proton energy, as an estimator of the neutrino energy ($E_{had} = E_\mu + E_p$).

In Ref. [1], the capabilities of ND280 upgrade in measuring the STVs have been presented. Notably the δp_T measurement (the STV quantifying the difference between the muon and proton momenta in the plane transverse to the neutrino direction) allows a direct probe of the Fermi momentum and an estimation of the non-QE component. Such measurement is made possible by the improved ND280 upgrade detector, lowering the proton threshold enough to cover the relevant phase space for QE interactions, and the identification of a STV ($\delta\alpha_T$) able to constrain FSI effects on protons with very good precision. Thus, to fully exploit the potential of the new proton-related variables, a multidimensional analysis is needed and, consequently, large statistics to populate all the relevant phase space. As an example, we report in Fig. 38, the statistical uncertainty for a $p_n, E_{had}, \delta\alpha_T, E_{rec}$ analysis as a function of collected POTs at the ND280 upgrade. The different phase space regions enable a clean measurement of Fermi momentum and binding energy (through p_n) in the bulk of the events, a clear sensitivity to non-QE events (e.g. when $E_{QE} < E_{had}$) and coverage in phase space corners with atypical behavior ($E_{QE} > E_{had}$) limiting the model-dependent extrapolations. Indeed, the inclusion of hadron variables in the analysis allows to extend the tuning of the nuclear models to an unprecedented precision and to benchmark them with a multi-variable parametrization extracted from data. The average (statistical-only) uncertainty in such multidimensional analysis, as shown in Fig. 38, is expected to reach 5% at the end of T2K-II.

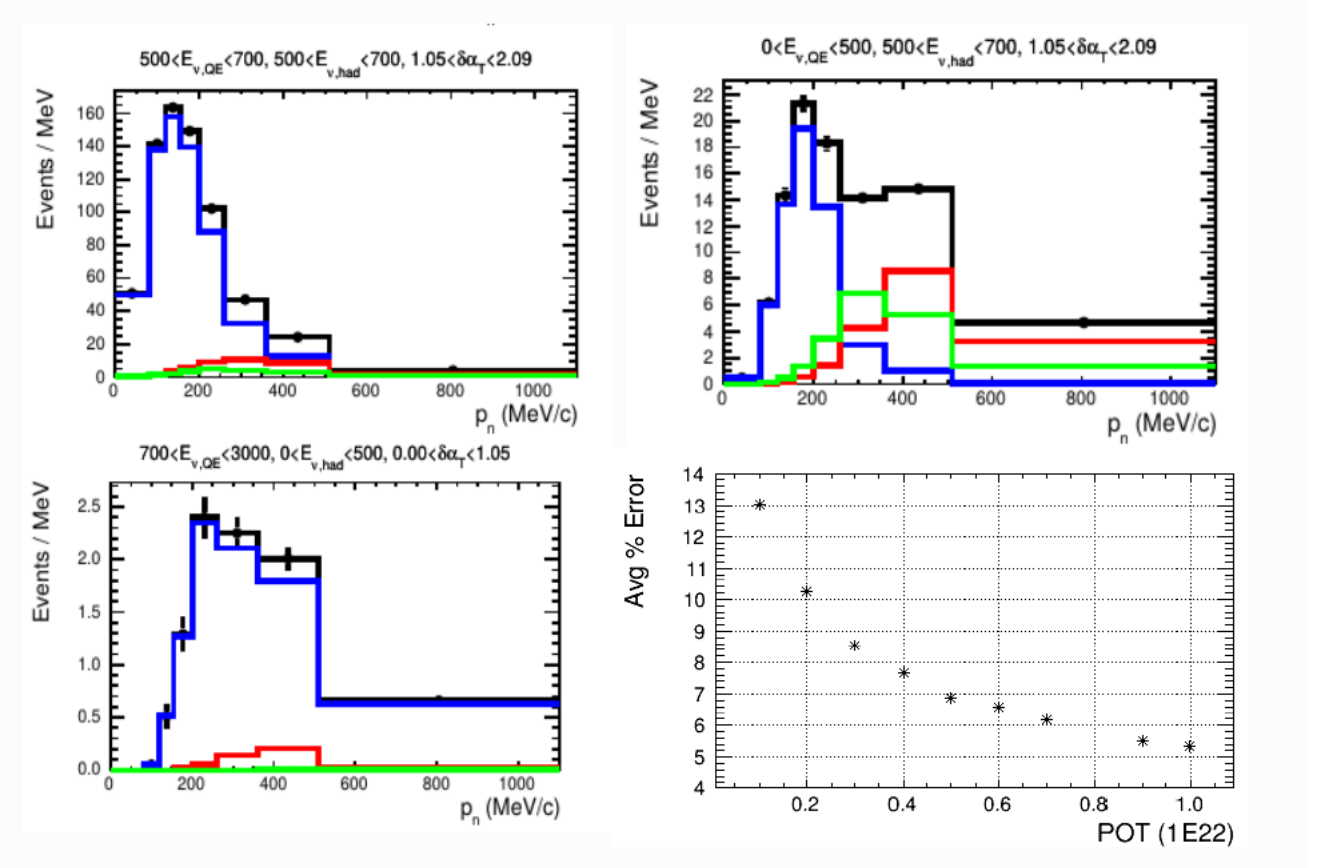


Figure 38: Example of multidimensional analysis in bins of p_n , E_{had} , $\delta\alpha_T$, E_{rec} with statistical errors for 10^{22} POTs. CCQE events (blue line), 2p2h events (red line) and pion production with FSI absorption (green line) are shown separately. The statistical uncertainty averaged over all the bins is shown as a function of the collected POTs.

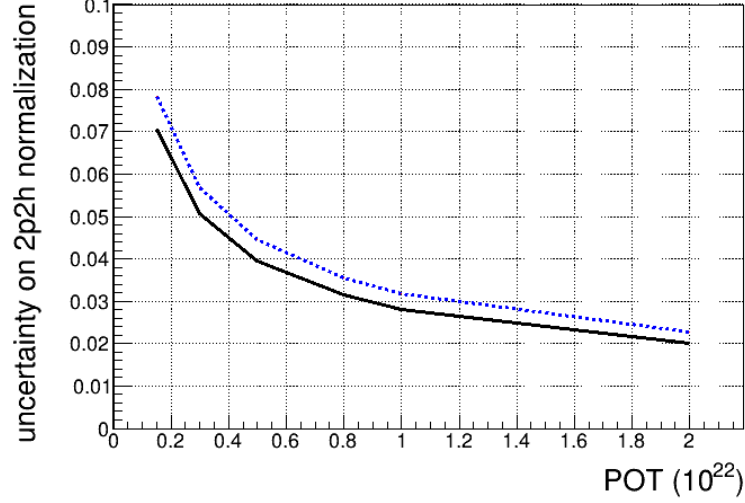


Figure 39: Precision on the ND280 upgrade constrain on the contribution from multinucleon interactions (2p2h) as a function of the POT by performing a fit in δp_T versus $\delta \alpha_T$. Two options are tested for the uncorrelated bin-by-bin uncertainty: 1% (black line) and 10% at 8×10^{20} scaled proportionally to the POTs (dashed blue line).

4.2.1 REDUCTION OF KEY MODEL UNCERTAINTIES

In order to estimate quantitatively the impact of Super-FGD measurements using low momentum protons on the systematic uncertainty for the oscillation analysis, a simplified analysis has been performed. The simulation described in Ref. [1] has been used to parametrize the efficiency and resolution of muon and proton reconstruction at the ND280 upgrade. A likelihood binned fit has been built including the most relevant systematic uncertainties, as of today. The capability to constrain the non-QE contribution to the zero-pions final state, analysing the lepton-proton kinematics in the plane transverse to the neutrino direction, is shown in Fig. 39: the results of the fit in δp_T versus $\delta \alpha_T$ are reported. The normalization of QE and non-QE (both multinucleon interactions, also called 2p2h, and pion production followed by absorption through FSI) are left free in the fit. The QE shape is left free in 100-MeV bins for QE events in the bulk of the δp_T distribution (< 300 MeV) and the relative normalization of 2p2h above and below 600 MeV in δp_T is also left free. Dedicated studies in T2K have shown that this an effective way to describe the uncertainty on the kinematics of the nucleon-nucleon pair in the initial state. A 30% prefit uncertainty on proton FSI is applied (constrained at % level after the fit). An overall normalization uncertainty of 3.7% is applied, assuming 3% from flux, 2% from detector modeling and 1% from background subtraction. It should be noted that, with the statistics available at T2K-II and the huge amount of information available in the multidimensional analysis, the overall normalization uncertainty has very small impact on the results. On top of the statistical uncertainty, two options have been tested for the bin-by-bin uncorrelated uncertainty: an uncertainty of 1% (simulating the impact of flux, detector and background systematics) or a very conservative uncertainty of 10% at 8×10^{20} p.o.t. scaled proportionally to the POTs (assuming a very poor prior knowledge on the nuclear model). In both cases the contribution of 2p2h (pion FSI) can be estimated with few % ($\sim 2\%$) precision with 10^{22} POT.

In Fig. 40 the new variable E_{had} is compared to E_{rec} , used today in T2K and based only on the lepton kinematics. The first is clearly a more precise estimator of the true neutrino energy and therefore a more powerful variable to estimate the binding energy. In Fig. 41 the results of a fit of p_n versus E_{had} to extract the binding energy is shown. p_n is a very good estimator of Fermi momentum which exploits also the kinematic of the final state in the longitudinal direction (parallel to the neutrino). Therefore, on top of the uncertainties already mentioned in the very conservative option above, the full flux uncertainty as of today (from the T2K prefit covariance matrix) is included and the binning in p_n

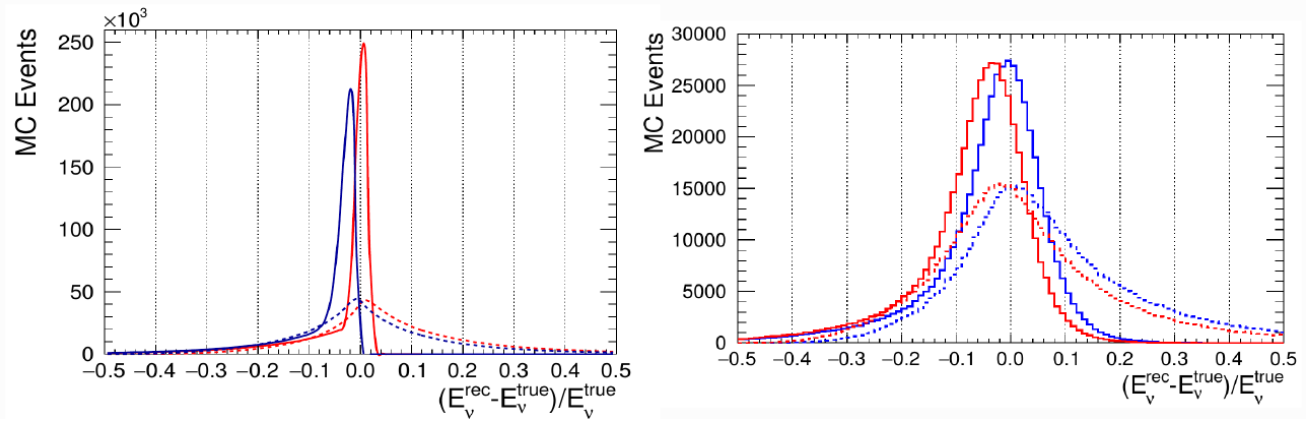


Figure 40: Comparison of neutrino energy reconstruction in QE events using the new variable $E_{had} = E_p + E_\mu$ (solid lines) or E_{rec} , based only on muon kinematics (dashed lines). Two different values of binding energy are compared and the distributions without detector effects (left) and after detector smearing and efficiency (right) are shown.

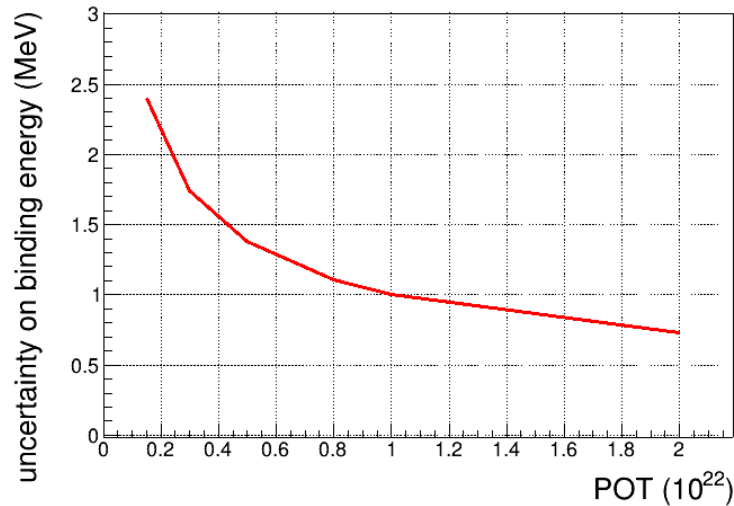


Figure 41: Precision on the ND280 Upgrade constrain on the binding energy as a function of POT by performing a fit to p_n versus E_{had} .

and E_{had} has been made much coarser, with respect to the statistics available, to adapt to the available estimation of flux uncertainty. Even with this very conservative assumptions, a precision on binding energy of about 1 MeV can be obtained with 10^{22} POT.

Similar measurements of STV and E_{had} can be made using incoming antineutrinos thanks to the ND280 Upgrade capability of detecting neutrons. The Super-FGD is large enough to collect, in most of the events, the energy deposited by the first collision of neutrons along their path, allowing a neutron detection efficiency of around 60%. A detailed discussion of neutron simulation and detection in an Super-FGD-like detector can be found in [17]. In terms of statistics, a measurement of average neutron multiplicity with few % precision at the T2K neutrino energy is possible, as shown in Fig.42. The ND280 upgrade performances on neutron reconstruction are more difficult to predict, with respect to protons, since this kind of measurement has not yet been performed in T2K. A dedicated test beam has been done at Los Alamos laboratories in December 2019, in order to benchmark the predictions from the simulation reported in Ref. [1]. The difference in time between the signals at the interaction vertex and at the neutron interaction point allows to estimate the neutron momentum, from its time of flight, with a resolution of about 15%. A pessimistic 5% is assumed for the background rate, including neutrons produced out of the fiducial volume, photons and secondary neutrons. Using this assumption,

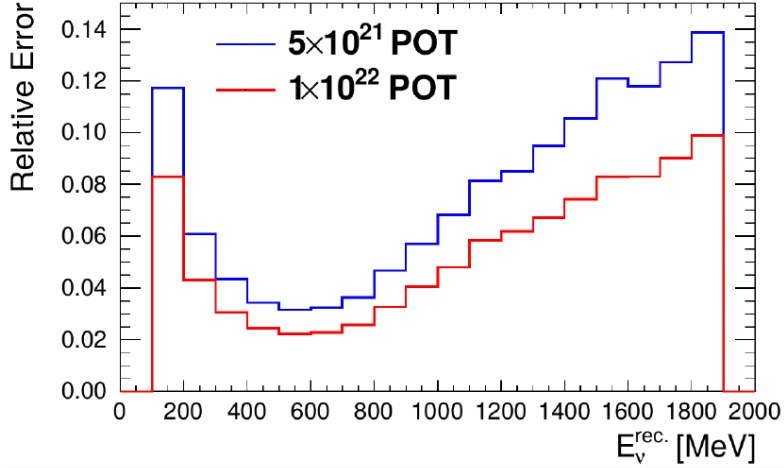


Figure 42: Statistical uncertainty on the neutron multiplicity measurement with ND280 Upgrade as a function of the reconstructed neutrino energy.

a similar analysis of STV has been performed for antineutrino, showing in general a worsening of a factor of ~ 2 with respect to the neutrino results. Despite the worse sensitivity, such an analysis may allow a characterisation of how nuclear effects can be different for neutrinos and antineutrinos, which may prove important when interpreting the differences between observed neutrino and antineutrinos event rates in oscillation analyses in terms of CP-violation.

In summary, at 10^{22} POT we can expect a constrain on the non-QE contribution (both 2p2h and pion FSI separately) of better than 3% (6%) and a constrain on the binding energy at MeV (few MeV) level for neutrino (antineutrino) interactions. In these studies we assumed conservative uncertainties and the present knowledge of nuclear effects. We expect that the huge amount of data and lepton-proton information collected by T2K-II will allow a significant step forward in the comprehension of nuclear effects relevant as systematics uncertainties for the oscillation measurements. The T2K-II data will be highly informative to design the next-generation of analysis and identify the sub-percent systematic uncertainties in the run to the ultimate precision.

4.2.2 ANTI-NEUTRINO ENERGY RECONSTRUCTION FROM $\bar{\nu}_\mu$ INTERACTIONS ON HYDROGEN

The recent analysis in Ref. [17] reports a method of anti-neutrino energy reconstruction for charged-current meson-less interactions in an Super-FGD-like detector which is largely free of the aforementioned poorly understood nuclear effects that usually distort and bias attempts to measure neutrino energy. The method is based on the event-by-event measurement of the outgoing neutron kinetic energy, something the Super-FGD is well suited to, and the subsequent assessment of the momentum imbalance on the plane transverse to the incoming anti-neutrino direction to separate neutrino interactions on hydrogen from those on carbon in the Super-FGD hydrocarbon scintillator.

As briefly discussed in Sec. 4.2.1, the momentum of neutrons ejected from the target nucleus of a neutrino interaction can be identified by measuring the time between the interaction (using another of the interaction's products) and a neutron re-interaction inside the Super-FGD. If this is done for antineutrino charged-current pion-less interactions, the neutron's momentum and direction can then be used to form δp_T . Such a sample of events will be dominated by CCQE interactions, which occur on both the carbon and the hydrogen of the Super-FGD plastic scintillator. The carbon portion of δp_T is expected to be similar to what is seen in neutrino interactions, but since interactions on hydrogen contain no nuclear effects, the hydrogen component will always give $\delta p_T = 0$. This is shown for interactions in a detector similar to the Super-FGD before and after the consideration of a realistic simulation of detector effects in Fig. 43. By cutting on δp_T to isolate a hydrogen enriched sample of

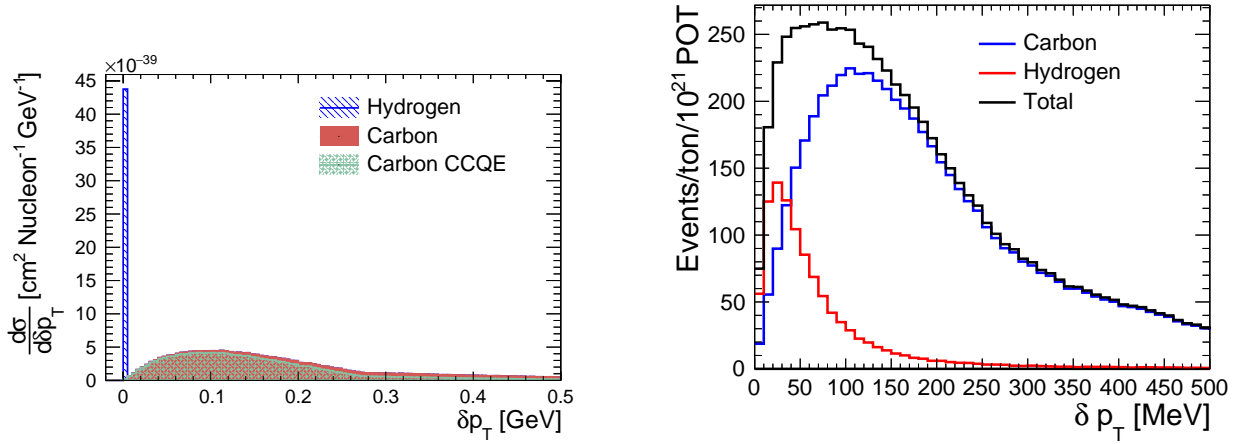


Figure 43: Taken from [17]. **Left:** The differential cross-section for $CC0\pi$ interactions on a hydrocarbon target as a function of δp_T for anti-neutrino interactions from the T2K experiment's anti-neutrino flux according to the NEUT 5.4.0 simulation. The cross-section is split by the target nucleus and whether or not the interaction is CCQE or not (only for carbon, as all $CC0\pi$ interactions on hydrogen are CCQE). No detector smearing or acceptance effects are considered. **Right:** The NEUT 5.4.0 predicted event rate of $CC0\pi$ interactions from the T2K anti-neutrino flux at a Super-FGD-like detector as a function of δp_T obtained after applying the detector smearing effects. Events are separated based on the target nucleus of the neutrino interactions.

events (where even the carbon background, having low δp_T , tends to be from events that were minimally impacted by nuclear effects) from which it will be possible to reconstruct the antineutrino energy in a way that is much less dependent on poorly understood nuclear effects. This is demonstrated, including the simulation of detector effects, in Fig. 44.

This method has the potential to provide around a factor of two improvement in anti-neutrino energy reconstruction and may be used to build a constraint on the incoming neutrino flux's normalisation and shape, potentially providing an important constraint in future oscillation analysis. Although this approach seems promising, it should be noted that careful study of the remaining carbon background will be required (perhaps through comparisons of δp_T for neutrino and antineutrino interactions).

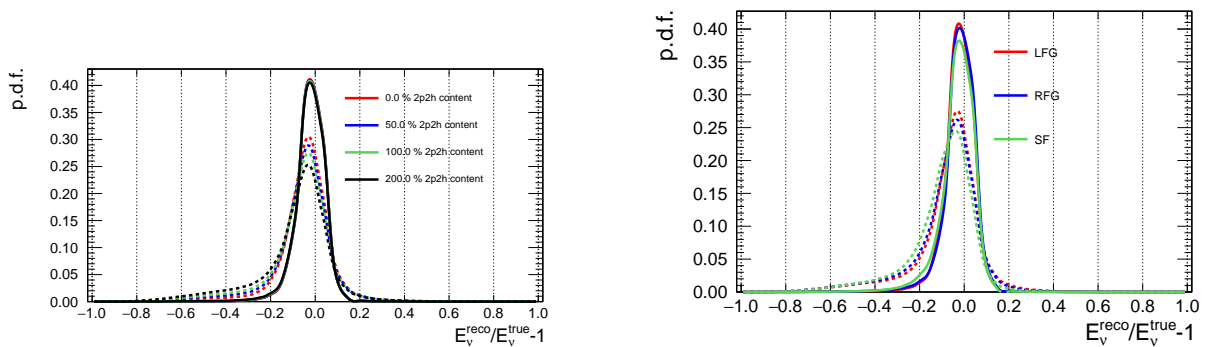


Figure 44: Taken from [17]. The anti-neutrino energy resolution before (dashed lines) and after (solid lines) applying cuts on δp_T (10 cm and 50 MeV) for variations on the NEUT 5.4.0 simulation. **Left:** The line colours correspond to different normalisations of the $2p2h$ component. **Right:** The line colours correspond to different initial state nuclear models.

4.2.3 IMPROVEMENTS ON ν_e/ν_μ UNCERTAINTY

Another key uncertainty for the oscillation analysis, particular for the electron neutrino appearance channel and therefore for measurements of the PMNS CP-violating phase, is the difference between electron and muon neutrino cross sections. First of all, the radiative corrections are larger for electrons than for muons, but this effect is in principle calculable [18]. The impact of the different multiplicity of emitted photons and their effect on the selection efficiency and electron/muon identification can be evaluated, and corrected for, by implementing the photon emission in Monte Carlo. Further uncertainties are due to how lepton mass effects couple to the nucleon form factors [7] and to nuclear effects such as FSI and Pauli blocking (see for example Refs. [19, 20]). The form factor effects causes a ν_e/ν_μ cross-section uncertainty of around 3% whilst the nuclear effects remain poorly understood, contributing at least a few % integrated uncertainty but having much more pronounced effects in kinematic regions of low momentum and energy transfer. It is possible that these uncertainties will become dominant in future oscillation analyses.

The best way to constrain the ν_e/ν_μ cross-section uncertainty would certainly be to measure directly the electron neutrino cross-sections using the intrinsic electron neutrino component of the T2K beam but, despite the notable improvements the Super-FGD could bring to such an analysis, it is likely that the statistical precision on a such a measurement would not allow a ν_e/ν_μ cross-section uncertainty of better than $\sim 4\%$. However, ND280 upgrade is well placed to be able to probe the physics at the source of these uncertainties. As discussed in the introduction to Sec. 4.2, ND280 Upgrade will have access to high statistics samples of exclusive scattering data with a low proton momentum tracking threshold which will enable novel constraints on the nuclear effects that drive part of the ν_e/ν_μ cross-section uncertainty. Techniques similar to what is described in Sec. 4.2.2 are able to isolate a sample of neutrino-hydrogen interactions from which the nucleon form factors could be analysed, thus potentially providing additional constraints on the remaining part of the ν_e/ν_μ cross-section uncertainty.

References

- [1] K. Abe et al. “T2K ND280 Upgrade - Technical Design Report”. In: (2019). arXiv: [1901.03750](#).
- [2] D. Attié et al. “Performances of a resistive MicroMegas module for the Time Projection Chambers of the T2K Near Detector upgrade”. In: *Nucl. Instrum. Meth.* A957 (2020), p. 163286. arXiv: [1907.07060](#).
- [3] K. Abe et al. “Search for CP Violation in Neutrino and Antineutrino Oscillations by the T2K Experiment with 2.2×10^{21} Protons on Target”. In: *Phys. Rev. Lett.* 121.17 (2018), p. 171802. arXiv: [1807.07891](#).
- [4] Arie Bodek and Tejin Cai. “Removal Energies and Final State Interaction in Lepton Nucleus Scattering”. In: *Eur. Phys. J. C* 79.4 (2019), p. 293. arXiv: [1801.07975](#).
- [5] J. Nieves, I. Ruiz Simo, and M.J. Vicente Vacas. “Inclusive Charged-Current Neutrino-Nucleus Reactions”. In: *Phys. Rev. C* 83 (2011), p. 045501. arXiv: [1102.2777](#).
- [6] K. Abe et al. “Measurement of the charged-current electron (anti-)neutrino inclusive cross-sections at the T2K off-axis near detector ND280”. In: (Feb. 2020). arXiv: [2002.11986](#).
- [7] Melanie Day and Kevin S. McFarland. “Differences in Quasi-Elastic Cross-Sections of Muon and Electron Neutrinos”. In: *Phys. Rev. D* 86 (2012), p. 053003. arXiv: [1206.6745](#).
- [8] Juan Nieves and Joanna Ewa Sobczyk. “In medium dispersion relation effects in nuclear inclusive reactions at intermediate and low energies”. In: *Annals Phys.* 383 (2017), pp. 455–496. arXiv: [1701.03628](#).

- [9] E.S. Pinzon Guerra et al. “Using world charged π^\pm –nucleus scattering data to constrain an intranuclear cascade model”. In: *Phys. Rev. D* 99.5 (2019), p. 052007. arXiv: [1812.06912](#).
- [10] T. Ovsianikova et al. “New experiment WAGASCI to measure cross sections of neutrino interactions in water and hydrocarbon using J-PARC beam”. In: *Phys. Part. Nucl.* 48.6 (2017), pp. 1014–1017.
- [11] K. Abe et al. “Measurement of neutrino and antineutrino oscillations by the T2K experiment including a new additional sample of ν_e interactions at the far detector”. In: *Phys. Rev.* D96.9 (2017), p. 092006. arXiv: [1707.01048](#).
- [12] K. Abe et al. “Characterization of nuclear effects in muon-neutrino scattering on hydrocarbon with a measurement of final-state kinematics and correlations in charged-current pionless interactions at T2K”. In: *Phys. Rev. D* 98.3 (2018), p. 032003. arXiv: [1802.05078](#).
- [13] X.G. Lu et al. “Measurement of final-state correlations in neutrino muon-proton mesonless production on hydrocarbon at $\langle E_\nu \rangle = 3$ GeV”. In: *Phys. Rev. Lett.* 121.2 (2018), p. 022504. arXiv: [1805.05486](#).
- [14] M. Elkins et al. “Neutron measurements from antineutrino hydrocarbon reactions”. In: *Phys. Rev. D* 100.5 (2019), p. 052002. arXiv: [1901.04892](#).
- [15] X. G. Lu et al. “Measurement of nuclear effects in neutrino interactions with minimal dependence on neutrino energy”. In: *Phys. Rev. C* 94.1 (2016), p. 015503. arXiv: [1512.05748](#).
- [16] Andrew P. Furmanski and Jan T. Sobczyk. “Neutrino energy reconstruction from one muon and one proton events”. In: *Phys. Rev. C* 95.6 (2017), p. 065501. arXiv: [1609.03530](#).
- [17] L. Munteanu et al. “A new method for an improved anti-neutrino energy reconstruction with charged-current interactions in next-generation detectors”. In: (2019). arXiv: [1912.01511](#).
- [18] A. De Rujula, R. Petronzio, and A. Savoy-Navarro. “Radiative Corrections to High-Energy Neutrino Scattering”. In: *Nucl. Phys. B* 154 (1979), pp. 394–426.
- [19] Alexis Nikolakopoulos et al. “Electron versus Muon Neutrino Induced Cross Sections in Charged Current Quasielastic Processes”. In: *Phys. Rev. Lett.* 123.5 (2019), p. 052501. arXiv: [1901.08050](#).
- [20] Artur M. Ankowski. “Effect of the charged-lepton’s mass on the quasielastic neutrino cross sections”. In: *Phys. Rev. C* 96.3 (2017), p. 035501. arXiv: [1707.01014](#).